TITLE: Visual projection neuron convergence and compensation in developing sensorimotor circuits in the *Drosophila* optic glomeruli

AUTHOR NAMES AND AFFILIATIONS:

Brennan W. McFarland[1], HyoJong Jang[1], Natalie Smolin[1], Tanja A. Godenschwege[2], Aljoscha Nern[3], Yerbol Z. Kurmangaliyev[4], Catherine R. von Reyn[1,5]

[1]School of Biomedical Engineering, Science and Health Systems, Drexel University, Philadelphia, PA

[2]Department of Biological Sciences, Florida Atlantic University, Boca Raton, FL

[3]Janelia Research Campus, HHMI, Ashburn, VA

[4]Department of Biological Chemistry, Howard Hughes Medical Institute, David Geffen School of Medicine, University of California, Los Angeles, Los Angeles, CA

[5]Department of Neurobiology and Anatomy, Drexel University College of Medicine, Philadelphia, PA

ABSTRACT:

Visual features detected by the early visual system must be combined into higher order representations to guide behavioral decision. Although key developmental mechanisms that enable the separation of visual feature channels in early visual circuits have been discovered, relatively little is known about the mechanisms that underlie their convergence in later stages of visual processing. Here we explore the development of a functionally well-characterized sensorimotor circuit in *Drosophila melanogaster*, the convergence of visual projection neurons (VPNs) onto the dendrites of a large descending neuron called the giant fiber (GF). We find two VPNs encoding different visual features that target the same giant fiber dendrite establish their territories on the dendrite, in part, through sequential axon arrival during development prior to synaptogenesis. Physical occupancy is important to maintain territories, as we find the ablation of one VPN results in expanded dendrite territory of the remaining VPN, and that this compensation enables the GF to remain responsive to ethologically relevant visual stimuli. Our data highlight temporal mechanisms for visual feature convergence and promote the GF circuit, and the *Drosophila* optic glomeruli where VPN to GF connectivity resides, as an ideal developmental model for investigating complex wiring programs and plasticity in visual feature convergence.

INTRODUCTION:

For an animal to respond to visual stimuli in its environment, visual features encoded in parallel at the early stages of visual processing must be combined and integrated within higher-ordered brain regions, and then relayed to the appropriate motor circuits to initiate a behavioral response. Many developmental mechanisms that configure parallel information streams to

simultaneously extract multiple visual features across an animal's visual field have been uncovered (Schmucker et al., 2000; Millard et al., 2007; Fuerst et al., 2008; Nern et al., 2008; Sanes & Zipursky, 2010; Lefebvre et al., 2012; Zipursky & Grueber, 2013; Strother et al., 2017; Liu et al., 2020). However, the developmental mechanisms that configure circuits to then recombine extracted features are not well understood.

In vertebrates, one of the earliest convergence of visual features occurs at the level of the superior colliculus in mammals and optic tectum in non-mammals, where retinal ganglion cell input is transformed to motor outputs for eye movements and avoidance responses (Dhande et al., 2015; Bollmann, 2019). In invertebrates such as *Drosophila melanogaster*, one of the earliest occurrences is within the optic glomeruli in the central brain (Strausfeld et al., 2007; Wu et al., 2016).

The optic glomeruli contain the axon terminals from distinct cell types of columnar visual projection neurons (VPN) that project from the last two neuropil of the fly's optic lobes, the lobula and the lobula plate. Each of the 20+ VPN consist of multiple retinotopically distributed neurons that cover the fly's visual field and are hypothesized to encode distinct visual features (Strausfeld et al., 2007; Wu et al., 2016; Keles¸ & Frye, 2017; Klapoetke et al., 2017; Ribeiro et al., 2018; Klapoetke et al., 2022). Within its glomeruli, neurons of each VPN type form synapses with multiple synaptic targets, including descending neurons (DN) that project axons to the ventral nerve cord (VNC, the fly spinal cord homologue) where they in turn synapse onto interneurons and motoneurons that generate behavioral outputs (Hsu & Bhandawat, 2016; Louis & Simpson, 2018; Namiki et al., 2018). The VPN to DN connections and associated circuits within optic glomeruli are therefore the site of one of the earliest sensorimotor transformations in *Drosophila*. Unlike the olfactory glomeruli which have a predominantly one to one olfactory

receptor neuron to projection neuron mapping (Sakuma et al., 2014), the optic glomeruli are not dedicated to a single DN type. Instead, DN dendrites infiltrate multiple, semi-overlapping subsets of glomeruli (Namiki et al., 2018; Ache et al., 2019), essentially assembling VPN features into higher order, behaviorally relevant motor and premotor outputs. How this complex and precise wiring is established during development is presently unknown.

The large DN called the giant fibers receive major input from two VPN types in the optic glomeruli, lobula columnar neuron type 4 (LC4) and lobula plate lobula columnar neuron type 2 (LPLC2) (Figure 1A) (von Reyn et al., 2017; Klapoetke et al., 2017; Ache et al., 2019). LC4 and LPLC2 encode the angular velocity and angular size of an expanding object, respectively (von Reyn et al., 2017, Ache et al., 2019), and enable the GF to drive a rapid takeoff escape in response to an object approaching on a direct collision course (von Reyn et al., 2014). The GF circuit is well-suited for investigating the development and function of visual feature convergence as the connectivity in adult flies has been recently established through electron microscopy, genetic handles exist for the GF and its major input cell types, and the accessibility of the GF to electrophysiology enables the functional consequences, such as altered synaptic connectivity, of experimental manipulations during development to be evaluated (von Reyn et al., 2017; Zheng et al., 2018; Ache et al., 2019; Scheffer et al., 2020). GF dendrites also lie in close proximity to other VPN that are not synaptic partners in the adult, like lobula plate lobula columnar neuron type 1 (LPLC1), which provides an opportunity to investigate developmental interactions with both intended and unintended partners.

Here, we capitalized on this well-established sensorimotor circuit (von Reyn et al., 2014; von Reyn et al., 2017; Ache et al., 2019) to investigate how VPN inputs are wired into the GF across development. We screened VPN and GF driver lines for early developmental expression

and cell-type specificity. We then used identified drivers to visualize VPN and GF interactions across metamorphosis and identified timed interactions with intended partners with strong spatial stereotypy. Pairing a comprehensive scRNA-seq atlas of the developing *Drosophila* visual system (Kurmangaliyev et al., 2020) and labeling of synaptic proteins over development, we compared the time course of VPN to GF interactions with the arrival of synaptic machinery. To investigate VPN competition along GF dendrites, we genetically ablated one VPN cell type (LC4) and investigated both structural and functional compensation from the surviving VPN partner (LPLC2). Our data provides insight into the development of VPN pairing with DN and establishes the optic glomeruli as a genetically and functionally tractable model to uncover developmental mechanisms for visual feature integration.

RESULTS

Stereotyped connectivity between select visual projection neurons and the GF

GF lateral dendrites extend into the optic glomeruli in close proximity to multiple VPN cell-types (Figure 1A, B). EM reconstruction in a full adult fly brain (FAFB, Zheng et al., 2018) previously revealed that 55 LC4 and 108 LPLC2 neurons synapse directly onto the GF lateral dendrite, contributing 2,442 and 1,366 synapses, respectively (Ache et al., 2019). Along the lateral dendrite, VPN synapses are segregated across the medial-lateral axis, with LC4 predominantly localized to medial, and LPLC2 localized almost exclusively to the most lateral dendritic regions (Ache et al., 2019). To investigate stereotypy in VPN to GF connectivity, we utilized a second EM dataset of a *Drosophila* hemibrain (Scheffer et al., 2020; Clements et al., 2020). In this EM reconstruction, we found 71 LC4 and 85 LPLC2 neurons established 2,290 and 1,443 synapses onto the GF lateral dendrites, respectively (Figure 1C). We confirmed that

LC4 and LPLC2 synapses segregated along the medial-lateral axis, with only 2/85 LPLC2 neurons making 23 and 28 synapses, respectively, in predominantly LC4 occupied medial areas.

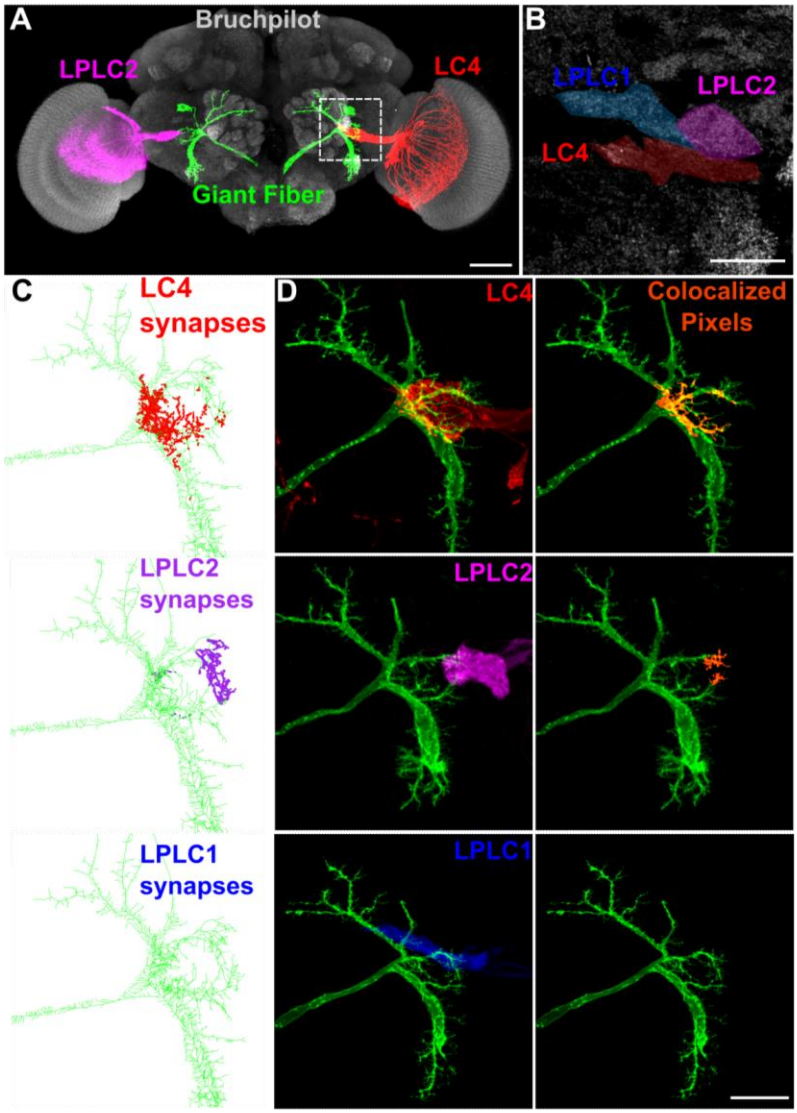

Figure 1. Select VPN are synaptically coupled to the Giant Fiber.
(A) Max intensity projections of GF (green), LPLC2 (magenta, one hemisphere), and LC4 neurons (red, one hemisphere) are superimposed over a neuropile label bruchpilot (brp), gray. A small ROI (dotted white box) highlights the section magnified in panel (*B*). Scale bar = 50µm.
(B) Max intensity projection of a sub-stack of brp labeling in the optic glomeruli (gray) with LPLC2 (magenta), LC4 (red) and LPLC1 (blue) glomeruli highlighted. Scale bar, 20µm.
(C) Drosophila hemibrain EM reconstruction of GF (green) with colored regions indicating input synapses from LC4 (red), LPLC2 (magenta) and LPLC1 (blue).
(D) (Left) Max intensity projections of dual labeled GF (smGFP-HA) and LC4 (top), LPLC2 (middle) or LPLC1 (bottom) (smGFP-V5). (Right) Colocalized pixels between GF and respective VPNs superimposed over GF max intensity projection. Scale bar, 20µm.

Since the EM data only represent connectivity within two fly brains, we investigated the consistency of this connectivity by examining contacts between GF and VPN membranes across multiple adult flies. We used two split-GAL4 driver lines that targeted all LC4 and LPLC2 neurons, respectively (Wu et al., 2016; von Reyn et al., 2014, von Reyn et al., 2017), and simultaneously labeled LC4 or LPLC2 and GF (Figure 1A, B, D). As a proxy for membrane contacts, we performed intensity-based thresholding on each cell-type of interest to generate representative masks, and then visualized colocalized regions along GF dendrites (Figure 1D). Similar to both EM datasets, we consistently observed LC4 contacts on the most medial regions of the GF lateral dendrites and LPLC2 contacts on the most lateral regions. We also found in 4 of 17 brain hemispheres, a small subset of LPLC2 neurons also extended into the most medial regions on the GF, as seen in the hemibrain EM dataset (Figure 1 – figure supplement 1, arrow) (Scheffer et al., 2020). These results suggest that LC4 and LPLC2 consistently segregate to stereotyped regions along the medial-lateral axis with rare exception.

As a negative control we used the same approach to assess the projection of LPLC1, a VPN that is adjacent to LC4 and LPLC2 and predicted to not synapse with the GF (Ache et al., 2019). As expected, no synapses were identified in the hemibrain EM dataset (Figure 1C), and no membrane contacts were observed between GF and LPLC1 across all adult flies (Figure 1D right). To further evaluate these contacts results, we employed GFP reconstitution across synaptic partners (GRASP) (Gordon and Scott, 2009; Feinberg et al., 2008), which allows visualization of contacts between adjacent membranes via reconstituted GFP expression (Figure 1 – figure supplement 2). Consistent with the EM dataset and our adult membrane contact results, we observed GFP expression between GF and LC4 and LPLC2 in medial/lateral

locations respectively, but not between GF and LPLC1. Taken together, our data further support that LC4 and LPLC2, but not LPLC1, are the major direct VPN inputs to the GF, and that LC4 and LPLC2 segregate along the GF lateral dendrite on the medial and lateral regions, respectively.

Although LPLC1 does not directly synapse with the GF, it synapses onto LC4 (226 synapses) and, to a lesser extent, LPLC2 (40 synapses) (Figure 1 – figure supplement 3) in the hemibrain EM dataset. Most of these inputs are to dendritic regions. Additionally, LC4, as well as LPLC2, synapse predominantly to LPLC1 dendrites (40 and 46 synapses, respectively), implying reciprocal connections. This is in agreement with previous EM studies identifying LPLC2 provides significant input (826 synapses) to LC4 dendrites and axons, and LC4 has reciprocal connections to LPLC2 (199 synapses) almost exclusively onto the axons (Ache et al., 2019). These data suggest that although LPLC1 does not directly synapse with GF, it may influence GF-mediated takeoff behavior or GF visual feature tuning indirectly through LC4 or LPLC2. In support of this, optogenetic activation of LPLC1 can evoke takeoff escapes, although at a lower probability than LC4 or LPLC2 (Wu et al., 2016). To evaluate information flow more directly from LPLC1 to the GF, we expressed red-shifted channelrhodopsin CsChrimson in LPLC1 using two separate driver lines, and light activated LPLC1 while recording from the GF using whole-cell electrophysiology. As a negative control, we also activated LC11 that is not synaptically coupled to these VPN or the GF. LPLC1 activation evoked significant responses in the GF (as compared to LC11 activation), but the response latency from the start of the light stimulus was significantly longer than LC4 to GF activation, which is consistent with LPLC1 indirectly activating the GF (Figure 1 – figure supplement 3).

The Giant Fiber lateral dendrites extend, elaborate, and then refine across pupal stages.

Prior developmental investigations into the GF have focused on axonal wiring with respect to post-synaptic interneuron and motor neuron partners in the ventral nerve cord (VNC) (Allen et al., 1998; Jacobs et al., 2000; Godenschwege et al., 2002; Murphey et al., 2003; Allen et al., 2006; Kennedy & Broadie, 2018). However, little is known about how GF dendrites develop in the central brain, and how GF-VPN interactions across development lead to the established territories on the GF dendrite in the adult (Phelan et al., 2008). Therefore, we next investigated GF and VPN development.

The GF is born during embryonic stages of development but does not generate neurites until the third instar larval stage (Allen et al., 1998). To label the GF at these early timepoints, we screened existing GF driver lines and identified a GF-LexA driver that turns on in late larval stages. We used this line to express a membrane targeted reporter (smGFP; Nern et al., 2015) in the GF and dissected pupae in 12-hour increments over metamorphosis. We focused on development of the GF lateral dendrites where VPN synapse (Ache et al., 2019) and quantified the total pixels occupied by the dendrite as a proxy for complexity and size. We also quantified the dendrite's length along the medial-lateral axis over time. In the first half of metamorphosis (24-48hAPF), the GF exhibited numerous filopodia, long thin protrusions without a bulbous head, and an increase in arbor complexity with the GF projecting between 3.1 $\pm$ 1.0 primary dendrites laterally (Figure 2A, B), a number that varied between animals and hemispheres. In addition, the dendrite length increased from 16.4 ± 3.8 µm at 24hAPF to 24.6 ± 3.3 µm at 48hAPF (n= 13 and 22, respectively) (Figure 2A, C). From 48hAPF to 60hAPF, the GF dendrites had the largest growth from 24.6 ± 3.3 µm to 30.3 ± 3.7 µm (Figure 2C).

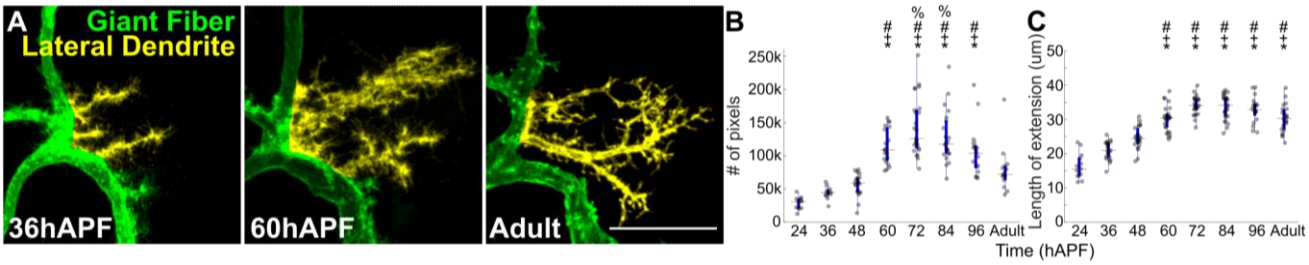

Figure 2. Time course of GF dendritic arbor extension.
(**A**) Max intensity projection of GF (green) at 36hAPF (left), 60hAPF (middle), and adult (right) with the lateral dendritic region highlighted in yellow at distinct developmental stages. Scale bar, 20µm. Images were first processed using a median filter to remove background noise in analysis. (**B**) Quantification of total number of GF lateral dendrite pixels from (A-C). An unpaired Kruskal-Wallis test was performed $p=1.3386\times10^{-18}$, followed by Dunn-Tukey-Kramer multiple comparison test, * indicates $p < .05$ significance compared to 24hAPF, + indicates $p <.05$ significance compared to 36hAPF, # indicates $p < .05$ significance compared to 48hAPF, and % indicates $p <.05$ significance compared to adult. $N \geq 12$ hemibrains from at least four flies (**C**) Quantification of length of lateral dendrite extension. An unpaired Kruskal-Wallis test was performed, $p=2.07201\times10^{-12}$, followed by Dunn-Tukey-Kramer multiple comparison test, * indicates $p < .05$ significance compared to 24hAPF, + indicates $p <.05$ significance compared to 36hAPF, # indicates $p < .05$ significance compared to 48hAPF.

In the early second half of metamorphosis (60-72hAPF), GF lateral arbor complexity and length peaked at 72hAPF (Figure 2 A-C), with the lateral dendrites extending 34.1 ± 2.7 µm (n=25). During this time, filopodia were still present, but visibly shorter than in the first half of metamorphosis. The number of primary and secondary dendrites remained varied between hemispheres and across animals, though there were many more secondary dendrites than in earlier stages (Figure 2A).

In the final stages of metamorphosis (72hAPF – eclosion), the complexity/size of the GF significantly decreased (Figure 2A, B), while the overall length was largely maintained from lengths observed at 72hAPF. Filopodia were no longer obvious, and branches appeared less complex and began to resemble the adult anatomy. These data also align with earlier investigations into GF axon development, where adult morphology was reached at ~100hAPF, just prior to eclosion (Allen et al., 2006).

Initial contacts between GF and VPNs are staggered in time.

We next investigated VPN axon targeting with respect to GF dendritic outgrowth. At present it is unknown when columnar VPN neurons are born (Courgeon and Desplan, 2019), but potentially these neurons arise after larval hatching, or in early pupal stages, a period when neuroblasts divide and give rise to other visual neurons (such as T4/T5) in the neighboring neuropil, the lobula plate (Mora et al., 2018). We hypothesized that VPN would commence outgrowth and partner matching in coordination with GF dendrite development. To visualize developmental interactions of select VPN and GF, we screened existing (Wu et al., 2016) as well as newly generated VPN split-GAL4 driver lines to identify ones that turned on early. We used these VPN lines and our GF LexA line to concurrently label select VPN cell-types (LC4, LPLC2, LPLC1) and GF over metamorphosis. We applied the method we developed and validated for quantifying VPN/GF colocalization using the known adult connectivity, with mask pixel colocalization serving as a proxy for membrane contacts.

Using an LC4 driver line GAL4 we identified to have early detectable marker expression ~18hAPF (referred to as LC4_4), we observed LC4 axonal extension and initial contact with GF at 24hAPF (Figure 3D). LC4 axons diverge, with the dorsal fraction projected near the dorsal branch of the GF lateral dendrite, and the ventral half projected more laterally towards the proximal regions of the GF (Figure 3 – figure supplement 1A). At 36hAPF, our LPLC2 and LPLC1 driver lines have turned on, though we did not observe any contact with the GF (Figure 3B, C, E, F). Contacts between the GF and LC4 continued to increase, with both dorsal and ventral fractions still apparent (Figure 3A, arrow, arrowhead, respectively).

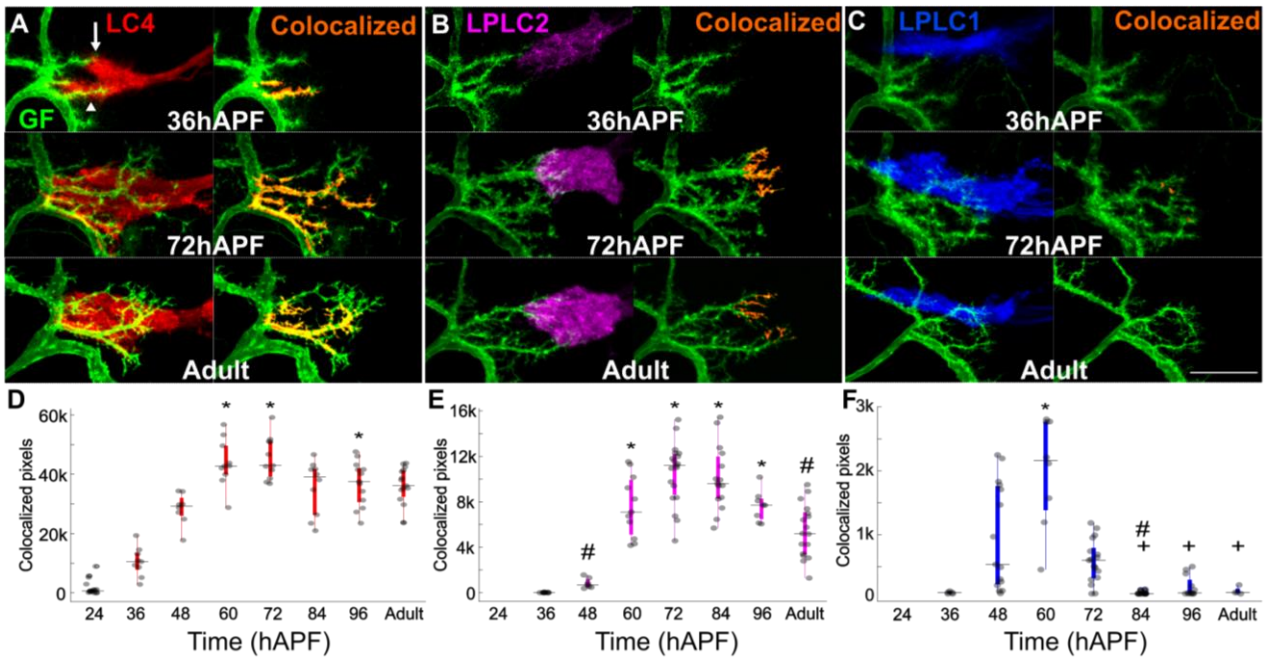

Figure 3. Time course of membrane colocalization between GF lateral dendrite and VPNs over metamorphosis.
(A-C) Left, max intensity projection images of GF membrane (green) with respect to LC4 (red, A), LPLC2 (magenta, B), and LPLC1 (blue, C) axonal membrane at distinct developmental stages. Right, max intensity projections of GF with VPN colocalized pixels (orange) superimposed along GF lateral dendrites. Scale bar, 20µm.
(D-F) Quantification of colocalization in (A-C) with colors corresponding to VPN type. An unpaired non-parametric Kruskal-Wallis test was performed (LC4, $p=2.08821 \times 10^{-12}$; LPLC2, $p = 1.98258 \times 10^{-10}$; LPLC1, $p = 1.59655 \times 10^{-8}$) followed by a Dunn-Tukey-Kramer multiple comparison test. *= $p<.05$ as compared to 36hAPF, $^{+}$= $p<.05$ as compared to 60hAPF, $^{\#}$= $p<.05$ as compared to 72hAPF. $N \geq 6$ hemibrains from at least three different flies.

At 48hAPF, LC4 and GF continued to show an increase in contacts (Figure 3D), and LC4 dorsal and ventral dendrites had converged. At this time, approximately 24 hours after initial GF/LC4 contact, we observed GF contact with LPLC2 (Figure 3B, E) as the ventral branch of the GF lateral dendrite extended parallel to but past the LC4 glomerulus, into the LPLC2 glomerulus (Figure 3 – figure supplement 1B, arrowhead). LC4 axons appeared more variable in shape, with fractions of LC4 axons deviating away from the collective bundle trajectory as contact area along the medial region of the dendrite. Interestingly, we also observed at this time contacts between GF and LPLC1, a non-synaptic partner in the adult fly (Figure 3C, F).

However, the number of LPLC1 contacts was relatively small as compared to LPLC2 and LC4 (Figure 3D-F, y-axis). Altogether, our data suggest that during the first half of metamorphosis, the GF is in a 'partner-matching' stage whereby it samples its environment for potential synaptic partners. Initial interactions with VPN are time dependent with LC4 contacting GF prior to LPLC2 and LPLC1, and initial contacts are strongly biased towards VPNs that are synaptically coupled to the GF in the adult.

In the later stages of metamorphosis (60hAPF-96hAPF), after initial contacts are made, a significant increase in contacts between all VPNs and GF at 60hAPF compared to 36hAPF (Figure 3D-F) was observed. The relative number of LPLC1 contacts, however, remained small. We investigated GF and LPLC1 contacts at 60hAPF using two additional LPLC1 driver lines and found minimal putative interactions with GF (Figure 3 - figure supplement 2). Around 72hAPF, the GF continued to increase contacts with LC4 and LPLC2, and contacts with LPLC1 decreased. At 84hAPF, contacts between the GF, and LC4 and LPLC2, were relatively stable, while contacts with LPLC1 decreased to become almost negligible.

We confirmed our results with a second intensity-based thresholding quantification method (Figure 3 – figure supplement 3). Taken together, these results suggest that in the second half of metamorphosis GF prioritizes dendritic outgrowth and enhances contacts with multiple VPN, but eventually refines and stabilizes contacts with appropriate VPN partners (LC4 and LPLC2) but eliminates contacts with inappropriate VPN partners (LPLC1).

Expression of select synaptic genes across key stages of metamorphosis

Although our contact data provide the time course for interactions between VPN axons and GF dendrites during development, they do not provide information on the timing of

synaptogenesis. We therefore investigated how our dendritic outgrowth and contact data time course aligned with the expression of pre-synaptic machinery. We used a comprehensive scRNA-seq atlas of the developing *Drosophila* visual system which profiled optic lobe neurons at multiple time points across metamorphosis and identified both global and cell type specific transcriptional programs (Kurmangaliyev et al., 2020). As developmental clusters corresponding to LC4, LPLC2, and LPLC1 had been identified in this dataset, we re-analyzed these data to determine when synaptic genes are upregulated in metamorphosis following initial GF and VPN partner matching. Profiling expression of presynaptic genes including those that are found in the SNARE complex (Megighian et al., 2013; Cho et al., 2010; Scholz et al., 2019; Davis et al., 2020), or play a role in synapse function (Davis et al., 2020), revealed that all pre-synaptic genes assessed (Brp, Syt1, Snap25, nSyb, Cpx, Syx1A) were significantly upregulated for all 3 VPNs in the second half of metamorphosis compared to 24hAPF (Figure 4A; Figure 4 – figure supplement 1). nSyb, Cpx, and Syx1A were upregulated as early as 36hAPF, Syt1 and Brp was upregulated as early as 48hAPF, and Snap25 was upregulated at 60hAPF (Figure 4A; Figure 4 – figure supplement 1). This upregulation follows the previously witnessed global neuronal expression pattern (Kurmangaliyev et al., 2020) and coincided with a significant increase in membrane contacts between GF and all VPNs, suggesting that synaptic machinery is being assembled across all VPN during this time.

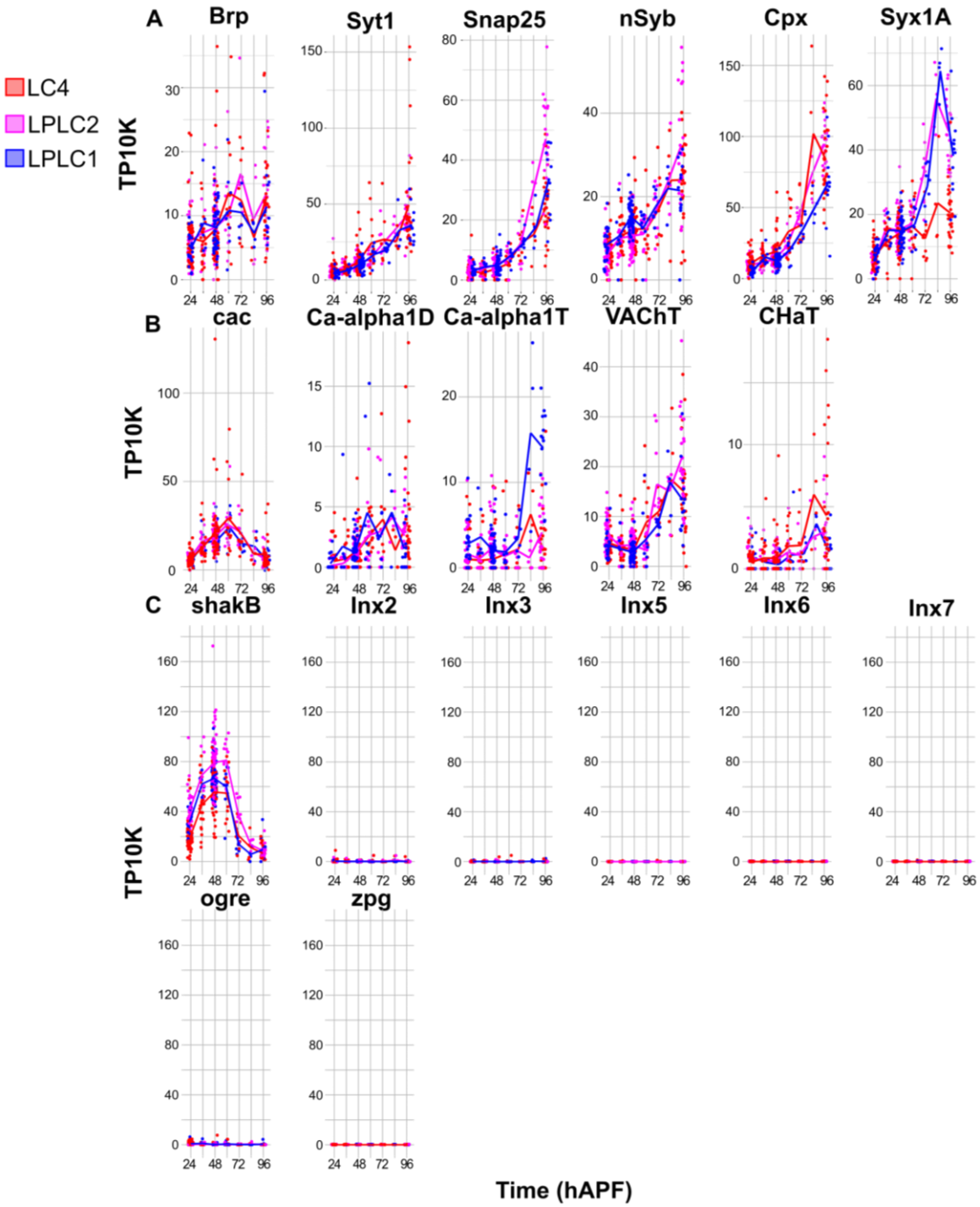

Figure 4. Time course of mRNA expression of presynaptic machinery and select channels in VPNs across metamorphosis.

(A) Expression of select pre-synaptic genes implicated in synaptic structure or function for LC4 (red), LPLC2 (magenta), and LPLC1 (blue) from 24 to 96hAPF.

(B) Expression of voltage gated Ca^{2+} channels for VPNs and genes related to cholinergic synapse function.

(C) Expression of all innexins

The three VPNs investigated here are predicted to be cholinergic (Davis et al., 2020), therefore we also investigated gene expression specific to cholinergic synapse function, including choline acetyltransferase (ChAT), an enzyme that catalyzes the synthesis of glucose and choline to form acetylcholine, and the vesicular acetylcholine transporter (VAChT) that allows the transport of acetylcholine into synaptic vesicles. We found that ChAT and VAChT were upregulated in the latest stages of metamorphosis (60-72hAPF to 96hAPF) (Figure 4B; Figure 4 – figure supplement 2) again following the time course of nearly every other cholinergic neuron (Kurmangaliyev et al., 2020). This upregulation coincides with the timing of significant refinement between GF and all VPNs, when dendritic complexity is decreasing and then stabilizing. These data suggest that cholinergic activity is not required for initial wiring of VPN to GF but may play an important role in refinement.

Given the significant role electrical synapses play across development, we next profiled expression data of all innexins. Shaking B (ShakB) has been denoted to be the predominant innexin over development (Kurmangaliyev et al., 2020), and we also observed a significant increase as early as 36hAPF compared to 24hAPF (Figure 4C; Figure 4 – figure supplement 2), with all other innexins showing minimal to no expression across metamorphosis (Figure 4 – figure supplement 3). ShakB expression peaked between 48-60hAPF, followed by a significant decrease from 60hAPF to 72hAPF for all cell types (Figure 4 – figure supplement 2). This decrease occurred as ChAT and VAChT increased, potentially marking the transition from electrical synaptic coupling to chemical synaptic coupling.

GF and VPN initial contacts occur before Patterned Stimulus-Independent Neural Activity (PSINA), witnessed calcium activity that plays a role in developmental wiring (Akin et al., 2019). We therefore expanded our analysis to investigate calcium channels that may

participate in this activity: Cacophony (Cac), Ca-alpha1T, and Ca-alpha1D (Figure 4B; Figure 4 – figure supplement 2). Cac, a pre-synaptic voltage-dependent calcium channel was significantly upregulated at 48hAPF compared to 24hAPF for all three VPN. Expression peaked at 60hAPF with a significant decrease in expression from 60hAPF to 96hAPF. While Cac expression decreased, the two other calcium channels, Ca-alpha1D (L-type calcium channel) and Ca-alpha1T (T-type calcium channel) show significant upregulation compared to 24hAPF (except for Ca-alpha1T in LC4). These data, along with a report that PSINA also progresses initially through a phasic period (55hAPF-65hAPF) to a turbulent period (70hAPF to eclosion) suggest that VPN express different calcium channels at distinct developmental periods that contribute to different patterns of calcium activity (Akin et al., 2019). Interestingly, the time course of Cac expression mirrors ShakB expression, suggesting these two may play a role in setting the activity patterns during the phasic period, as witnessed in vertebrate models (Crépel et al., 2007; Malmersjö et al., 2013; Smedler et al., 2022).

We also investigated the timing of synapse formation using a new iteration of Stochastic Tagging with Recombination (STaR) (Peng et al., 2018). This strategy enables us to induce RS recombinase expression under permissive temperatures and visualize LPLC2 and LC4 specific Brp, driven by its endogenous promotor, and tagged with smGdP-V5. Brp is homologous to the mammalian ELKS/CAST family of proteins and is a ubiquitous presynaptic active zone protein that facilitates neurotransmitter release (Wagh et al., 2006; Knapek et al., 2011). We used LPLC2 and LC4_4 driver lines and quantified the native fluorescence of V5-tagged Brp over metamorphosis (Figure 4 - figure supplement 4). Based on our mRNA data (Figure 4A), we expected to visualize a similar time course in Brp-V5 expression in LC4 and LPLC2 and observe a significant increase in Brp-V5 intensity in LC4 and LPLC2 at 48hAPF compared to 24hAPF.

Instead, significant Brp accumulation was observed in LC4 axon terminals at 36hAPF and in LPLC2 at 48hAPF (Figure 4 – figure supplement 4), similar to the staggered arrival times of LC4 and LPLC2 on the GF dendrite. However, because V5-tagged Brp expression is dependent on both the native Brp promoter and when our driver lines turn on, the differences in Brp appearance could also be due to the temporal differences in the driver lines. In all, these data suggest at least one component of presynaptic machinery is available during or shortly after initial VPN to GF contacts are made, but that chemical synapses become functional when components of cholinergic synapses are upregulated during the later stages of development.

LC4 and LPLC2 occupy distinct regions along the GF dendrite across metamorphosis

In the adult GF escape circuit, LC4 provides input to the medial regions on the GF lateral dendrites, whereas LPLC2 provides input to the most lateral regions (Figure 1). However, it is unknown if this medial-lateral segregation is established initially or arises over development. To address this, we used our membrane contact data from each time point across metamorphosis, and manually aligned our brains so that the GF lateral dendrite was parallel to the x-axis. Colocalized pixels were then summed along the x-axis, normalized to the length of the lateral dendrite, and averaged across all brains for each timepoint (Figure 5). Across all time points, a minimal overlap between LC4 and LPLC2 along the x-axis was seen; the peak density of contacts for LC4 consistently occupied the most medial regions on the GF lateral dendrite, and LPLC2 on the most lateral regions (Figure 5 A-C).

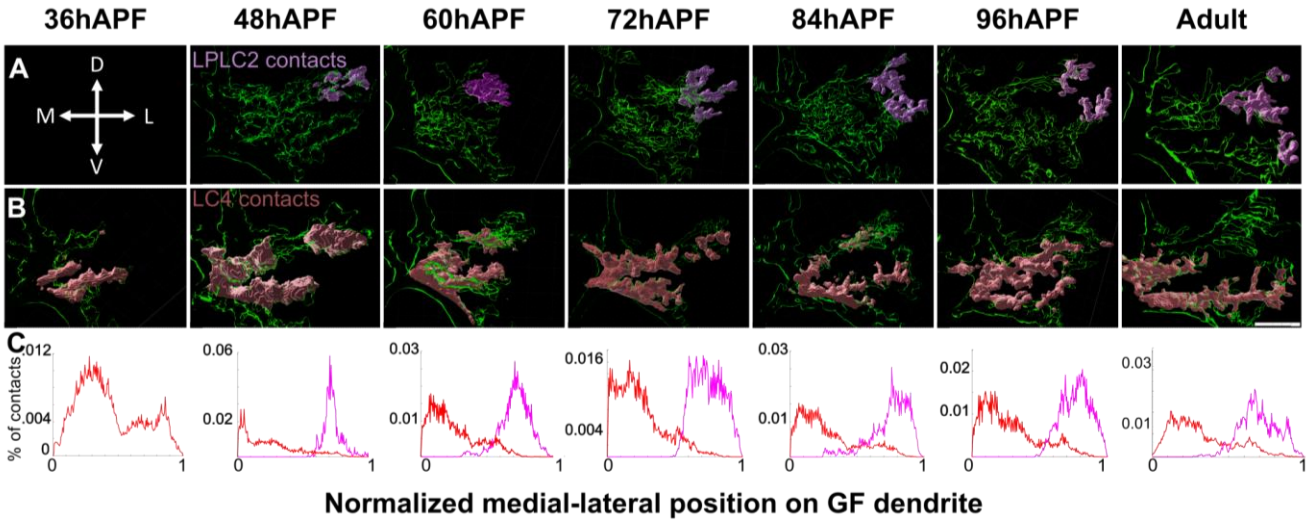

Figure 5. LPLC2 and LC4 occupy distinct regions on GF along the medial-lateral axis throughout all stages of development.
(A,B) 3D renderings (IMARIS) of GF lateral dendrites (green) with colocalized pixels with LPLC2 (A, magenta) or LC4 (B, red) superimposed at distinct timepoints during development. Scale bar, 10µm. D - dorsal, V – ventral, M – medial, L – lateral.
(C) Histogram of average percentage of VPN to GF dendrite colocalization along the normalized medial-lateral axis across development; colors used in plot for each VPN are matched to the same colors used for each VPN colocalization in (A, B).

As the lateral dendrite contains a ventral and a dorsal branch, the same analysis of these data was performed along the y-axis. Like the medial-lateral distribution, LC4 and LPLC2 contacts were biased to ventral and dorsal regions, respectively, though in the later stages of development (72hAPF – 96hAPF) these peaks were less segregated (Figure 5 – figure supplement 1). Interestingly, no obvious segregation of synapse localization along the dorsal-ventral axis was reported for a previous analyses of EM data (Ache et al., 2019). Given the small sample EM sample size, and differences between EM datasets, there may be variability across flies. Our results show that LC4 and LPLC2 initially target medial and lateral regions, and ventral and dorsal regions respectively, and maintain contacts in these respective locations throughout development.

LC4 ablation increases the GF contacts with the LPLC2 glomerulus

We next set out to investigate how VPN activity may contribute to the establishment of the medial-lateral localization of LC4 and LPLC2 inputs to the GF lateral dendrites. To test the hypothesis that LC4 activity potentially restricts LPLC2 terminals on the GF, we attempted to silence LC4 during development by expressing Kir2.1 (Pfeiffer et al., 2012; von Reyn et al., 2014) using our LC4_4 driver line. However, early expression of Kir2.1 resulted in the significant loss of LC4 in the adult, as quantified by cell body counts (Figure 6A; Figure 6 - figure supplement 1 A-D). However, expression with a distinct, late LC4 split-GAL4 line used in previous silencing experiments that has detectable marker expression between 24-36hAPF (von Reyn et al., 2017) (LC4_1) did not cause any significant decreases in LC4 cell body counts (Figure 6 – figure supplement 1 B, D). As our LC4_4 driver turns on ~18hAPF, prior to initial GF contact, and the LC4_1 driver has detectable marker expression after initial GF contact, our data suggest that overexpression of Kir2.1 early in development is detrimental to LC4 survival. Co-expression of an apoptosis inhibitor, p35 (Pecot et al., 2014), with Kir2.1 using the LC4_4 driver line did not prevent cell death (Figure 6 – figure supplement 1E, F), potentially due to redundancies in the apoptosis pathways.

As Kir2.1 was successful in killing the majority of LC4, we tested if the physical loss of LC4 had an effect on LPLC2 morphology and targeting. We expressed tdTomato in LPLC2 using a LexA driver line while simultaneously driving GFP or Kir2.1 in LC4 using our LC4_4. In adult flies lacking the majority of LC4, the LPLC2 axon bundle extended into areas where the LC4 glomerulus would be expected (Figure 6A), but there were no obvious differences in LPLC2 dendritic termination between experimental and control flies (data not shown). We next investigated the localization and density of contacts between GF and LPLC2 when LC4 was

killed (Figure 6B, C). We first identified the LPLC2 glomerulus using Brp as a neuropil label and manually traced the LPLC2 glomeruli to generate a mask (Figure 6B, C top row). We found that LC4 cell loss resulted in an LPLC2 glomerulus with altered structure as compared to control flies (Figure 6A, B, C). We then generated a mask of the GF and determined the area of overlap between the GF dendrites and LPLC2 glomerulus (Figure 6B, C middle and bottom row). We found that LC4 ablation significantly increased the number of contacts between GF and the LPLC2 glomerulus and that the contacts were localized to more medial regions of the GF dendrite (Figure 6B, C middle and bottom row, D). In summary, our data demonstrated LC4 ablation altered LPLC2 axonal morphology and increased GF dendrite arborizations within the LPLC2 glomerulus, suggesting the early arrival and physical presence of LC4 may impede LPLC2 from contacting more proximal regions of the GF.

We also expressed Kir2.1 in LC4 at later developmental stages with the LC4_1 driver line to determine if Kir2.1 silencing causes changes in LC4/GF membrane contacts. We found no significant difference in contacts between LC4 and GF whether we expressed Kir2.1 or GFP in LC4 (Figure 6E, F). Although this driver turns on later, it still expresses Kir2.1 prior to PISINA, suggesting LC4 targeting of the GF dendrite is activity independent. This further supports that LC4 and LPLC2 localization along the GF dendrite is established early due to the staggered timing of LC4 and LPLC2 contacts with the GF.

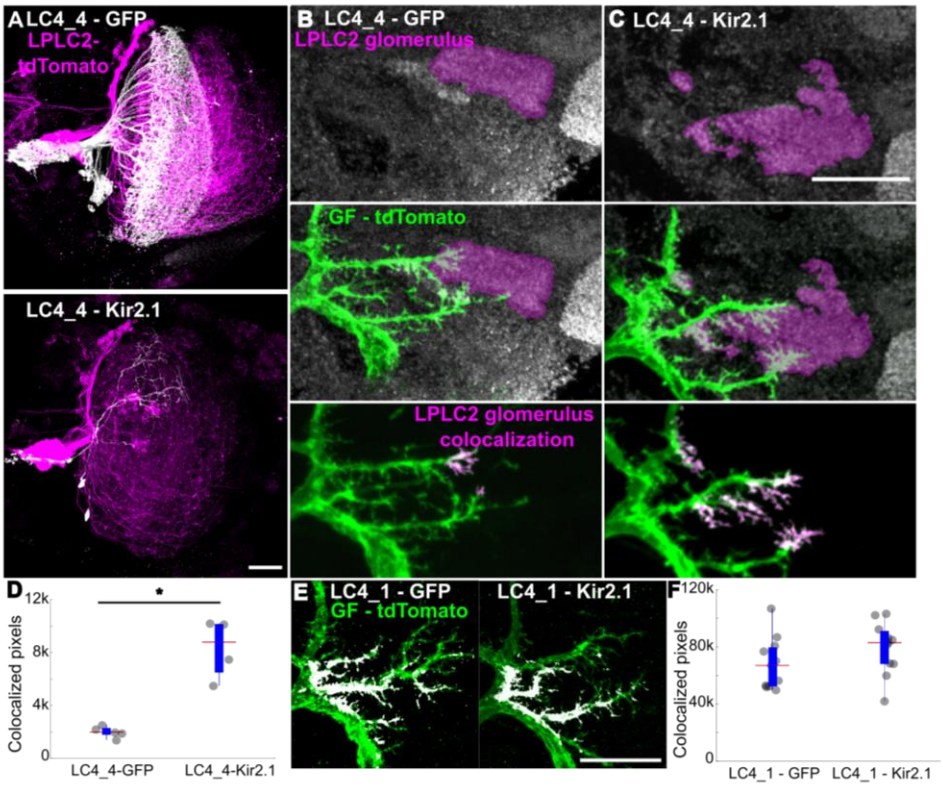

Figure 6. Kir2.1 induced LC4 cell death causes an increase in GF colocalization with LPLC2 glomerulus

(A) Max intensity projection images of LPLC2 expressing tdTomato (magenta) with LC4 (white) expressing GFP (top) or Kir2.1 (bottom) using LC4_4 that has detectable marker expression early in development. Scale bar, 20µm

(B,C) Top row: LPLC2 glomerulus (magenta) in a fly where the LC4_4 driver was used to drive GFP (B) or Kir2.1 (C) (grey, neuropil label). Scale bar, 20µm.

Middle row: GF dendrites (green, tdTomato) extending into the LPLC2 glomerulus.

Bottom row: Colocalized pixels (magenta) between GF and the LPLC2 glomerulus superimposed onto the GF (green).

(D) Quantification of colocalization between GF and LPLC2 glomerulus from (B,C). An unpaired non-parametric Mann-Whitney U-test was performed, $p = .0159$. $N \geq 4$ half brains

(E) Max intensity projection images of GF expressing smGFP (green) with colocalized pixels (white) between LC4 expressing GFP (left) or Kir2.1 (right) using the LC4_1 driver that turns on late during development. Scale bar, 20µm.

(F) Quantification of total colocalization in (E). An unpaired non-parametric Mann-Whitney U-test was performed, $p = .1486$. $N \geq 11$ half brains.

Functional compensation in the GF circuit after LC4 ablation

As our anatomical data suggest the loss of LC4 results in a reconfiguration of contacts between LPLC2 and GF, we next sought to understand how these reconfigurations may functionally alter GF integration of ethologically relevant visual stimuli. LC4 provides to the GF information about the angular speed while LPLC2 provides information on the angular size of an expanding object. Therefore, we reasoned with the loss of LC4, and the increase in contacts with LPLC2, the GF should lose components of its response attributed to LC4 (high angular velocity) and increase the magnitude of its responses attributed to LPLC2 that follow the size of an expanding object. We recorded GF responses in tethered, behaving flies using whole-cell patch clamp electrophysiology (Jang et al., 2022). We displayed looming stimuli to the fly where the known contributions of LC4 and LPLC2 have been established (von Reyn et al., 2017; Ache et al., 2019) (Figure 7A).

We found, as reported previously (von Reyn et al., 2017), that silencing LC4, by expressing Kir2.1 using the LC4_1 driver line, reduced the GF response to looming stimuli presented ipsilaterally to GF soma targeted for recordings (Figure 7B, C). However, the ablation of the majority of the LC4 population, by expressing Kir with the LC4_4 driver line, resulted in GF responses similar to or enhanced as compared the control (Figure 7B, C).Both silencing and ablating LC4 resulted in the absence of the short latency pop on response attributed to LC4 and predominantly observed with center and contralateral looming stimuli (von Reyn et al., 2017; Ache et al., 2019; Jang et al., 2022) (Figure 7B insets and 7D), which supports LC4 input are effectively diminished under both conditions. Our data suggest the witnessed compensation in GF response during LC4 ablation is due to the developmental reorganization of LPLC2.

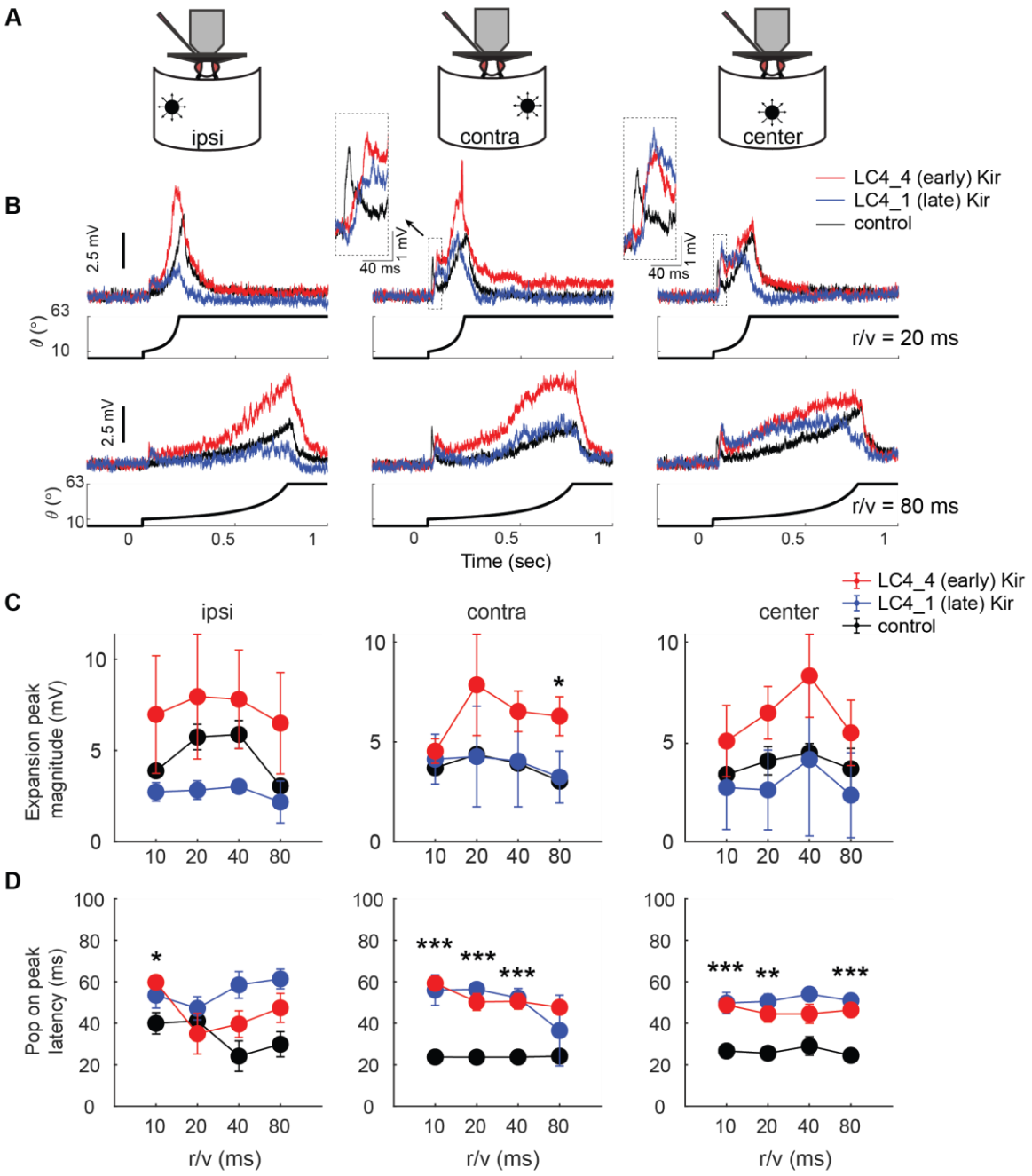

Figure 7. Compensation in the GF response to looming stimuli following Kir2.1 induced LC4 cell death

(A) Schematic depicting tethered fly presented with modeled visual stimuli at the ipsilateral side to the electrode (left), contralateral side (middle), or at the center (right).

(B) Looming stimuli trials with stimuli expanding fast (r/v = 10 ms) or more slowly (r/v = 80 ms). Inset images show magnified view near the onset to compare pop-on peak latencies between control, LC4_4 Kir, and LC4_1 Kir flies.

(C,D) Quantification of expansion peak magnitude and pop on peak latency. Error bars show mean ± SEM for control (black), LC4_4 Kir (red), and LC4_1 Kir (blue) flies, (ANOVA,

Tukey's Kramer post hoc, *=p<.05, **=p<.01, ***=p<.001, control n=5 flies, LC4_4 Kir n=4 flies, LC4_1 Kir n=3 flies), black asterisk from comparison between LC4_4 Kir and control flies.

Developmental schematic

In figure 8, we summarize our findings on the developmental time course for GF, LC4, LPLC2, and LPLC1 interactions. Our circuit schematic summarizes our membrane colocalization data (Figure 3) and is supplemented by scRNA-sequencing data (Figure 4).

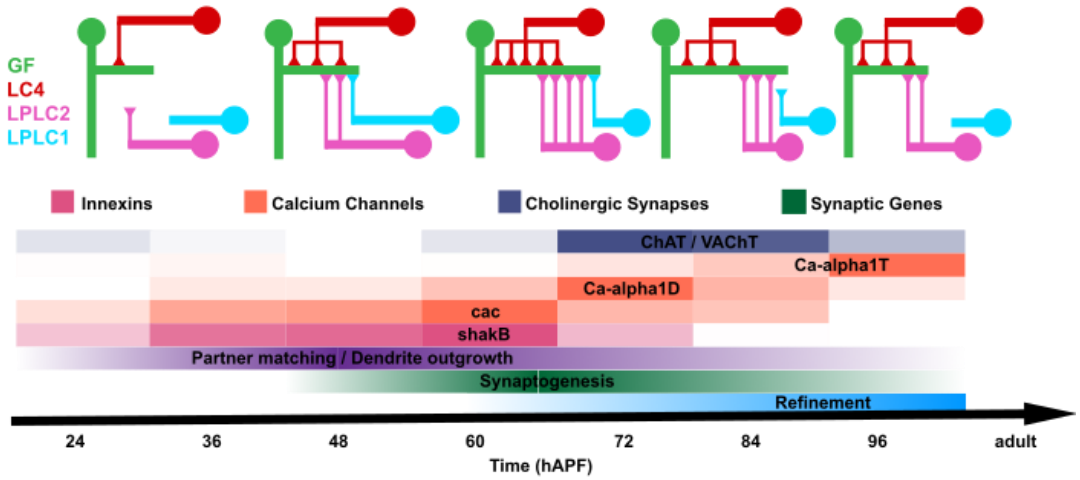

Figure 8. Schematic of GF and VPN development. GF and VPN interactions aligned to scRNAseq data and estimated developmental stages.

Discussion

Here, our investigation into the developmental interactions of GF dendrite and VPN axons supports a developmental program where GF and partner VPNs make initial contact in precise, stereotyped regions that are maintained into eclosion. As metamorphosis proceeds following initial contacts, GF dendrites arborize, extend, and increase contacts with VPNs, including a minority of unintended partners, coinciding with an upregulation in gap junctions, and the onset of PSINA (Akin et al., 2019). This outgrowth is followed by a period of refinement that coincides with an upregulation of cholinergic synaptic components, and different calcium channels are upregulated during the partner matching and refinement stages. Lastly, we report

the loss of a major VPN input leads to anatomical and structural changes that may translate to large functional changes in the circuit. Our data establishes the GF escape circuit as a sophisticated developmental model that can be used to study the integration of sensory inputs to a sensorimotor circuit and investigate the relationship between expressed genes and circuit development and function.

The development of the *Drosophila* visual system proceeds in a series of steps which likely serve to reduce the complexity of wiring paradigms from neurons of the same or neighboring cell-types, highlighting the importance of timing (Kolodkin & Hiesinger et al., 2017). We found with respect to the GF and correct VPN partners, LC4 contacts the GF approximately 24-36 hours prior to LPLC2. This could likely serve a similar functional purpose where staggered arrival of VPN axons could reduce the complexity of decisions made by the GF during partner matching, as is also seen in the olfactory glomeruli in an *ex-vivo* preparation (Li et al., 2021). From 36-72hAPF, we observe a coordinated increase in GF dendritic extension, arborization, and contacts with correct VPN partners, and incorrect VPN partners (Figure 3; Figure 3 – figure supplement 3). This coordinated period of outgrowth likely reflects a distinct mechanism to increase wiring robustness whereby the GF extends and elaborates to ensure all appropriate areas make contact in stereotyped dendritic regions. Our confocal data provide high-resolution confocal snapshots of membranes at distinct periods over metamorphosis, but as metamorphosis is a dynamic process, some dynamic or transient interactions may have been missed.

Localization of inputs onto dendrites determine dendritic computations and can confer special properties that are important for the function of the neuron in a circuit (Spruston, 2008; Gidon & Segev, 2012; Ferreira et al., 2020). In terms of connectivity, with respect to LC4 and

LPLC2, LC4 contacts medial GF dendritic regions, and LPLC2 to lateral regions. Our contact data suggests targeting of LC4 and LPLC2 to their respective regions is established during initial contact instead of being refined over development. Observed in the analogous olfactory glomeruli, PN-ORN targeting is also refined to a specific glomerulus (Jefferis et al., 2004; Berdnik et al., 2006), though following ORN ablation, partner interactions or glomerular structure is not affected (Berdnik et al., 2006). It is possible specific ligand-receptor interactions result in specificity in LC4 and LPLC2 targeting (Yogev & Shen, 2014; Sassoè-Pognetto & Patrizi, 2017; Sanes and Zipursky, 2020; Chowdhury et al., 2021), as shown in the olfactory glomeruli (Hong et al., 2012). Alternatively, with LC4 contacting the GF first in medial regions, it may physically inhibit LPLC2 from extending into medial regions, leaving it segregated to only the lateral tips. This may explain why LPLC2 extends into more medial regions following LC4 cell-death (Figure 6), but, it does not fully replace where LC4 normally occupies, suggesting segregation may arise from a combination of physical restraints from LC4 and potentially other neurons, in addition to molecular interactions. Similar as described for perturbing neural activity in the antennal lobe (Singh et al., 2010; Nakashima et al., 2019), cell-death of most LC4 neurons may alter neural activity patterns thereby inducing cell-type specific changes in synaptic gene expression and rearrangement of inputs to GF dendrites. It does not appear that activity-based mechanisms drive localization of LC4 and LPLC2 to specific regions because expression of Kir2.1 using a late (~36hAPF) LC4-driver line does not result in significant changes in LC4/GF contact density or localization (Figure 6E, F). In addition, elimination of most of LC4 neurons did not affect targeting of the remaining LC4 neurons to the GF dendrites in the expected regions.

In addition to a change in GF colocalization with the LPLC2 glomerulus, we also report altered GF output to looming stimulus presentatifon following LC4 cell-death (Figure 7), likely to preserve an evolutionary conserved escape behavior that is critical to the fly's survival. Because LC4, LPLC2 and LPLC1 share reciprocal connections between themselves (Figure 1 – figure supplement 3) and given that elimination of post-synaptic neurons can result in changes in GF anatomy (Hill, 2012; Kennedy & Broadie, 2018), it is difficult to predict where in the circuit this change comes from. Because we observe a significant increase in GF to LPLC2 connectivity, our prevailing hypothesis is that LPLC2 synaptic inputs to GF have increased. Alternatively, the 1-4 LC4 that remain after ablation may also have increased synaptic input, however the absence of LC4 pop on responses, and the limited visual field coverage with just 1-4 LC4 neurons suggests this would not underlie the enhanced GF responses.

The expression profile of genes over development can help describe the progression of stages of development (Sanes & Zipursky, 2020). Our GF and VPN colocalization shows a developmental progression that begins with partner matching between VPN and GF, and transition to a period of significant growth where GF dendrites extend and increase in complexity while also increasing contacts with both correct and incorrect partners. Following this significant growth, contacts are refined, and incorrect partners are eliminated as neurons assume their adult morphology. Comparison of the time course of scRNA-seq data to our membrane development provided insight into genes that may play a role in these processes. For example, during partner matching, synaptic maturation is synchronously upregulated at the transcriptomic level, however, the time course expression of recognition molecules is less synchronized and more cell-type specific (Kurmangaliyev et al., 2020). One hypothesis would be that expression of appropriate binding partners is cell-type specific and temporally regulated; LC4 upregulates recognition

molecules during initial GF/LC4 partner matching, and downregulates these molecules while LPLC2 upregulates recognition molecules, allowing for stepwise pairing on medial and lateral GF dendritic regions, respectively. ShakB, the predominant innexin across pupal development (Figure 4 – figure supplement 1), along with Cacophony (Cac), a calcium channel localized to pre-synaptic terminals, are upregulated in the first 60 hours of metamorphosis and decrease from 60-96hAPF. Calcium imaging in the developing optic lobe reveal PSINA beginning around 58hAPF; prior to this period activity is sparse and asynchronous (Akin et al, 2019). As GF and VPNs grow and increase contacts with one other until ~60hAPF, it is possible electrical activity and calcium transients may serve a role in these processes (Vonhoff & Keshishian, 2017; Luhmann & Khazipov, 2018). The time points ~60-72hAPF also may be a significant transitional period as we see the decrease of ShakB and Cac, and the beginning of refinement of VPN connectivity that coincides with the documented emergence of a PSINA transition from synchronous, patterned transients to turbulent activity that continues through eclosion. Following a significant increase in GF arborization, extension, and colocalization with VPNs, we observe a shift from 72hAPF-eclosion where the circuit refines. This period coincides with a significant upregulation in cholinergic related synaptic genes, ChAT and VAChT (Figure 4 – figure supplement 2-3), and select calcium channels (Ca-alpha1D, Ca-alpha1T). Given the well documented roles activity plays in circuit refinement (Faust et al., 2021), it is possible PSINA, cholinergic activity, or calcium activity play an active or permissive role driving refinement in late metamorphosis. Collectively, this data supports previously published results found across many systems where the progression from sporadic and infrequent firing, to synchronous, to turbulent activity results from emergence of electrical and chemical synapses (Kutsarova et al., 2017; Luhmann & Khazipov, 2018; Akin et al., 2019; Pan & Monje, 2020; Choi et al., 2021;

Faust et al., 2021). Our model system is well poised to investigate the role of electrical and chemical signaling, as well as specific genes, in circuit development and function.

While we here document the development of visual feature convergence on one DN dendrite, our work does not take into consideration any retinotopic arrangement that may exist. Once visual information leaves the optic lobe via VPNs, retinotopy seems to be lost (unlike in vertebrate systems (Sanes & Zipursky, 2010; Kolodkin & Zipursky, 2017), therefore a prevailing hypothesis is that most of the stimuli processing occurs before it reaches descending neurons and spatial information is secondary to specific response properties of VPN cell-types (Wu et al., 2016). More recent evidence demonstrates post-synaptic neurons could bias synaptic input strength depending on their receptive field to represent spatiotemporal information (Morimoto et al., 2020), and preliminary evidence suggests LC4 inputs to other descending neurons (DNP02, DNp04, DNp11), and other VPNs like LC6 (Morimoto et al., 2020) may follow a similar mechanism (Peek, 2018). If so, it would be interesting to look at and when and how these biases arise during development.

In summary, our data provides a detailed description of GF and VPN development, scRNA-sequencing data describing time course of many genes in coordination with GF/VPN development, and adaptation in response to LC4 cell-death. Our system has many advantages, cell-type specific genetic tractability being one of the most useful that enables sophisticated experiments, in addition to scRNA-sequencing data available over VPN development that can help inform molecular investigations. Our model is also unique in that two inputs appear to compete for dendritic space, providing a complex sensorimotor model to the field that will be useful to determine the relationship between connectivity, sensorimotor integration, and post-synaptic output. The GF also samples from other brain regions outside of the optic glomeruli

(Pézier et al., 2016), and it would be interesting to characterize the development of GF with respect to these other regions and further investigate how these inputs influence GF output. Finally, these VPN are only a few of the 20+ VPN that terminate in the optic glomeruli, and GF is one of hundreds of descending neurons providing the opportunity to investigate whether other descending neurons and VPNs develop over a similar time course.

Materials and Methods

Fly genotypes and rearing

All fly genotypes are listed in supplementary table 1. Stocks and experimental crosses were reared on a traditional molasses, cornmeal, and yeast diet (Archon Scientific), maintained at 25°C and 60% humidity on a 12-hour light/dark cycle, except for optogenetics experiments where dark reared flies were raised on 0.2 mM retinal food as larva and switched to 0.4 mM retinal food following eclosion. All experiments were performed on pupa (developmental staging protocol described below) or adult female flies 2-5 days post-eclosion.

Developmental staging

Pupal staging across developmental time points has been previously described (Wu and Luo, 2006). In brief, the sex of white pre-pupa was identified, and females were transferred to a separate petri dish, marked as 0 hours after pupa formation (hAPF), and reared for the appropriate amount of time before dissection. Dissections were performed within a 2-hour window of an identified pupal developmental stage. All pupal dissections were synchronized and processed through immunohistochemistry protocols for pixel intensity measurements of images.

Immunohistochemistry

All dissections were performed in cold Schneider's insect media (S2, Sigma Aldrich, #S01416) within a 15-minute window before solution exchange to avoid tissue degradation. Brains were then transferred to a 1% paraformaldehyde (20% PFA, Electron Microscopy Sciences, #15713) in S2 solution and fixed overnight at 4°C while rotating. Immunohistochemistry was performed following as described previously (Nern et al., 2015). Primary and secondary antibodies used in each experiment, along with respective concentrations, can be found in Supplementary Table 1. Following immunostaining, brains mounted onto poly-L-lysine (Vendor, CAS #) coated coverslips were then dehydrated in increasing alcohol concentrations (30, 50, 75, 95, 100, 100) for 5 minutes in each, followed by two 5-minute Xylene clearing steps (Fisher Scientific, #X5-500). Coverslips were mounted onto a prepared slide (75 x 25 x 1mm) (Corning, #2948-75X25) with coverslip spacers (25 x 25 mm) (Corning, #2845-25) placed on each end of the slide to prevent brain compression. Brain mounted slides were left to dry for at least 48 hours prior to imaging.

Confocal Microscopy

Unless otherwise stated, all images were taken on an Olympus Fluoview 1000 confocal system. Images were taken with a 60x, 1.42 NA oil immersion objective to achieve a voxel size of .103µm x .103µm x .45µm. Imaging parameters were minimally adjusted between images when imaging neuron membranes to achieve an image that utilizes the full pixel intensity range without oversaturating pixels. This was necessary as driver lines in earlier pupal developmental periods showed lower levels of expression than in later pupal developmental stages, therefore we adjusted imaging parameters that optimized membrane signal-to-noise ratio for each

developmental stage that would allow for optimized mask generation used in image analysis. In analyses where we quantified and compared pixel intensity across pupal developmental stages, all imaging parameters were kept consistent across all images. STaR images were taken on a Zeiss LSM 700 with a 63x, 1.4 NA oil immersion objective to achieve a voxel size of .06µm x .06µm x .44µm. Imaging parameters were kept consistent to allow for comparison across all samples.

Electron Microscopy

The publicly available electron microscopy hemibrain dataset (version 1.2.1) (Scheffer et al., 2020) was used in this paper. NeuPrint (Clements et al., 2020) was used to create renderings and connectivity diagrams.

Image analysis across development

Unless otherwise stated, no image processing prior to image analysis was performed. Only the brightness and contrast were adjusted to highlight neuronal processes when preparing images for figure generation. To quantify membrane colocalization between GF and VPN neurons across development, intensity-based thresholding was first used to generate a binary mask of each neuron membrane. Using a custom GUI written in Matlab, threshold values were manually selected to include processes of each cell-type and exclude background and regions of the neuron that were out of focus in each z-plane. Generated binary masks were inspected to make sure each mask was representative of the imaged neuron membrane channel. In certain cases, the set threshold did not include very fine neurites that were difficult to discriminate from background. Lowering threshold values to capture these processes in the mask would result in

background being included into the mask as well, therefore the final sum of pixels may be underestimated due to loss of some of these finer processes in the mask. Using these masks, colocalized pixels were collected plane-by-plane across the entire image stack using Boolean operators between GF and VPN masks. This output matrix results in a z-stack only where GF and VPN membranes are colocalized. This was used as our analysis pipeline for GF / VPN membrane contact localization. In some images, GF membrane labeling had a low SNR and prevented accurate mask generation and were therefore excluded from analyses. In select cases, non-GF and non-VPN cell-types would be labeled with the driver lines that we were unable to exclude in mask generation, therefore these data were excluded from analyses. To increase rigor, a second method to quantify GF to VPN membrane colocalization was used. Confocal stacks of labeled neuronal membranes were 3D rendered in Imaris using the Surfaces function. Thresholds were manually applied to generate 3D masks of neuronal membranes so that the rendered 3D image was representative of the imaged membrane. Similar to Matlab thresholding, in certain cases the set threshold did not include fine neurites as they were difficult to discriminate from the background using automated algorithms. Following initial 3D membrane renderings, we inspected each rendering compared to the confocal images and manually filled in regions using the 'Magic Wand' function where faint processes were still visible but not detected in the thresholding pipeline. Once 3D rendering was complete, we implemented the Surface-Surface contact area XTension which outputs a 3D rendering of only colocalized regions between the two input 3D membrane renderings. The volume of this output was quantified.

To determine where VPN contacts were localized on the GF lateral dendrite, a z-projection of the GF was manually aligned and rotated using anatomical landmarks consistently observed to align the lateral dendrite along the x-axis. The same rotation and alignment were

applied to the appropriate membrane colocalization matrix. An ROI was then drawn around the GF lateral dendrites, with anatomical landmarks consistently observed used to denote the beginning and end of the lateral dendrite. To account for variation in the lateral dendrite extension across images, we normalized the x-axis to the length of the drawn ROI (i.e., GF lateral dendrite). To determine where VPN contacts were localized on the GF lateral dendrite along the y-axis, the same images were used, but normalized the y-axis to the length of the drawn ROI. Total colocalized pixels were summed along each column or row, respectively, and the pixel density for each column or row was averaged across brains in each condition, then plotted along the normalized axis.

To quantify the average pixel intensity of VPN-specific Bruchpilot (Brp) puncta across developmental timepoints, VPN masks were generated from the membrane channel using the same pipeline used for the GF and VPN membrane colocalization. These binary masks were then multiplied to the Brp-puncta channel to gather raw pixel intensities for Brp-V5 puncta localized to the VPN membrane. The total intensity sum of the glomerulus was divided by the total number of membrane localized pixels to calculate the average pixel intensity.

Kir2.1 cell death and GF dendrite localization

To quantify LC4 cell death following early expression of Kir2.1, we performed immunohistochemistry against a GFP conjugated to Kir2.1 or GFP (controls), and Brp. Following confocal imaging, we manually counted LC4 cell bodies using the eGFP-Kir2.1 or GFP channel. To quantify GF dendrite density within the LPLC2 glomerulus following LC4 cell death, we used Brp to visualize the optic glomeruli active zones. Axons that make up each

individual glomerulus reliably terminate in the same region of the central brain, allowing us to consistently identify the LPLC2 glomerulus and determine glomerular boundaries.

scRNA-seq data analysis

To quantify changes in mRNA expression over development for our cells of interest, we used a recently published scRNA-seq dataset (Kurmangaliyev et al., 2020). For each developmental stage for each population, we performed an unpaired non-parametric Kruskal-Wallis test by ranks.

Electrophysiology

For whole-cell electrophysiology, female flies were head fixed to recording plates via UV glue, antenna were UV-glued, and the front legs were removed at the level of the femur as described previously (Jang et al., 2022, von Reyn et al., 2017). GFP positive GF soma were accessed for recordings by removing the cuticle and overlying trachea, and then removing the perineural sheath by local application of collagenase (0.5% in extracellular saline). The brain was perfused with standard extracellular saline (103 mM NaCl, 3 mM KCl, 5 mM *N*-Tris (hydroxymethyl)methyl-2- aminoethane-sulfonic acid, 8 mM trehalose, 10 mM glucose, 26 mM NaHCO3, 1 mM NaH_2PO_4, 1.5 mM $Cacl_2$ and 4 mM $MgCl_2$, pH 7.3, 270–275, bubbled with 95% O2/5% CO2 and held at 22°C). Recording electrodes (3.5-6.2 MΩ) were filled with intracellular saline (140 mM potassium aspartate, 10 mM HEPES, 1 mM EGTA, 4 mM MgATP, 0.5 mM Na_3GTP, 1 mM KCl, 20 μM Alexa-568-hydazide-Na, 260-275 mOsm, pH 7.3). Recordings were acquired in whole-cell, current clamp mode, digitized at 20kHz, and low pass filtered at 10kHz. All data were collected using Wavesurfer, an open-source software

(https://www.janelia.org/open-science/wavesurfer) running in MATLAB. Recordings were deemed acceptable if a high seal was attained prior to break through, the resting membrane potential was ≤ −55 mV, and the input resistance was > 50 MΩ. Current was not injected to hold the membrane potential at a particular resting level, and traces were not corrected for a 13mV liquid junction potential (Gouwens & Wilson 2009).

Optogenetics

Light activation of VPN cell types expressing CsChrimson (Klapoetke et al., 2014) while recording from GF was performed by delivering light (635 nm LED, Scientifica) through a 40x objective focused on a head fixed fly. Light pulses (5ms, 1.7 mW/cm^2 as measured in air at the working distance of the objective) were delivered 5 times at 30 second intervals.

Visual Stimuli

Visual stimuli were projected on a cylindrical screen surrounding a head fixed fly during whole-cell electrophysiology following the protocol described previously (Jang et al., 2022, Goodman 2018). 4.5-inch diameter mylar cylindrical screen covered 180° in azimuth and we used two DLP projectors (Texas Instruments Lightcrafter 4500) to minimize luminance attenuation at the end of the screen edge. The projections from the two projectors were calibrated on the cylindrical screen surface as described previously (Goodman et al., 2018) and the two projections were overlapped 18° in azimuth at center of the screen and blended for uniform illumination. Generated looming stimuli based on the equation (Gabbiani et al., 1999) below and constant velocity expansion stimuli were displayed with 912 x 1140 resolution in 6bit grayscale at 240 Hz which is above the flicker fusion frequency of *Drosophila* (100 Hz, Niven et al.,

2003). Looming stimuli are generated by simulating 2D projection of an object approaching at a constant velocity which mimics approaching predator. The angular size (θ) of the stimulus subtended by the approaching object and it is calculated over time (*t*) by the following equation (Gabbiani et al., 1999):

$$\theta(t) = 2tan^{-1}\left(\frac{r}{vt}\right)$$

where $t<0$ before collision and $t=0$ at collision for an approaching object with a half size (r) and constant velocity (v). Four looming stimuli (r/v= 10, 20, 40, 80ms) were displayed, starting at 10°, expanding to 63° and then held for 1 second. We presented each stimulus once per trial, in a randomized order, every 30 seconds. For each fly, two trials of the entire set of stimuli were averaged.

Data analysis and Statistics

We did not perform a power analysis prior to statistical analysis. For boxplots, the dividing line in the box indicates the median, the boxes contain the inner quartile range, the notches give the 95% confidence interval, the lines extending beyond the box include 95% of the data, and the dots beyond those lines are outliers. We first performed a Kolmogorov-Smirnov test for normality and determined our data did not follow a normal distribution. To compare changes across development, an unpaired non-parametric Kruskal-Wallis test by ranks was used and followed by a Dunn-Tukey-Kramer multiple comparison test at an alpha value of .05. For cases where statistical analysis was performed between two groups, an unpaired non-parametric Mann-Whitney U-test was performed. Significance values are reported in figure legends.

Supplementary Table 1: Fly genotypes and antibodies used in each figure

Figure	**Panel(s)**	**Driver Line(s)**	**Reporter transgene(s)**	**Antibodies**
Fig 1A.	A,D	GF_1_LexA (A,D), OL0048B (A,D), LPLC1_1 (D), LC4_4 (A,D)	smGFP-UAS-HA, LexAop-V5	**1º AB:** mouse nc-82 (anti-Brp) (1:30). **2º AB:** 647 goat anti-mouse (1:400). Conjugate: DyLight anti-V5-550 (1:400). Conjugate: DyLight anti-HA-488 (1:400).
Figure 1- Figure Supplement 1		GF_1_LexA, OL0048B	smGFP-UAS-HA, LexAop-V5	Conjugate: DyLight anti-V5-550 (1:400).

				Conjugate: DyLight anti-HA-488 (1:400).
Figure 1- Figure Supplement 2	A-C	GF_1_LexA (GF)(A-C), LC4_4 (A), OL0048B (B), LPLC1_1 (C)	GRASP-LexAop-GFP11, UAS-GFP1-10; smGFP-UAS-HA, LexAop-V5	Conjugate DyLight anti-HA-550 (1:400) Conjugate: DyLight anti-V5-550 (1:400).
Figure 2	A	GF_1_LexA (GF)	smGFP-UAS-HA, LexAop-V5	Conjugate: DyLight anti-V5-550 (1:400).
Figure 3	A-C	GF_1_LexA (GF), LC4_4 (LC4) (A), OL0048B (B), LPLC1_1(C)	smGFP-UAS-HA, LexAop-V5	Conjugate DyLight anti-HA-550 (1:400) Conjugate: DyLight anti-V5-550 (1:400).
Figure 3. Figure Supplement 1	A,B	GF_1_LexA (GF), LC4_4 (LC4)	smGFP-UAS-HA, LexAop-V5	Conjugate DyLight anti-HA-550 (1:400)

				Conjugate: DyLight anti-V5-550 (1:400).
Figure 3. Figure Supplement 2	A-C	LPLC1_2(A), LPLC1_3(B), GF_1_LexA (A,B)	smGFP-UAS-HA, LexAop-V5 (A,B)	Conjugate DyLight anti-HA-550 (1:400) Conjugate: DyLight anti-V5-550 (1:400).
Figure 3. Figure Supplement 3.	A,B	GF_1_LexA (GF), LC4_4	smGFP-UAS-HA, LexAop-V5	Conjugate DyLight anti-HA-550 (1:400) Conjugate: DyLight anti-V5-550 (1:400).
Figure 4 – figure supplement 4	A,B	LC4_4(A), OL0048B (B)	smGdP-STaR	**1º AB:** DsRed anti-rabbit (1:200) **2º AB:**

				568 goat anti-rabbit (1:400) Conjugate: DyLight anti-V5-650 (1:200)
Figure 5.	A,B	GF_1_LexA, OL0048B, LC4_4	smGFP-UAS-HA, LexAop-V5	Conjugate: DyLight anti-HA-550 (1:400) Conjugate: DyLight anti-V5-550 (1:400).
Figure 6.	A-C, E	GF_1_LexA (B,C,E), LC4_4 (A-C, E), 75G12_LexA(LP LC2)(A), LC4_1 (E)	UAS-Kir2.1-2(A), UAS-Kir2.1-1(B,C); UAS-GFP (B,E); UAS-tdTomato (A)	**1º AB:** Chicken anti-GFP (1:1000) DsRed anti-rabbit (1:200) Mouse nc82 (anti-brp) (1:30) **2º AB:**

				488 goat anti-chicken (1:200) 568 goat anti-rabbit (1:400) 647 goat anti-mouse (1:400)
Figure 6. Figure Supplement 1		LC4_4 (LC4) (A, C, E, F), LC4_1 (B),	UAS-Kir2.1-1 (A,B,E,F); UAS-tdTomato (E); UAS-p35 (F); UAS-GFP (C)	**1º AB:** Chicken anti-GFP (1:1000) DsRed anti-rabbit (1:200) **2º AB:** 488 goat anti-chicken (1:200) 568 goat anti-rabbit (1:400)

Key Resources Table

REAGENT or RESOURCE	SOURCE	IDENTIFIER
Mouse anti-nc82	DSHB	CAT# - AB2314866
Rabbit anti-GFP	Life technologies	CAT# - A11122
Chicken anti-GFP	EMD Millipore	CAT# - AB16901
Rabbit anti-HA	Cell Signaling Technologies	CAT# - C29F4
Rabbit anti-DsRed	Takara Bio	CAT# - 632496
Alexa Fluor 488 goat anti-chicken	Invitrogen	CAT# - A11039
Alexa Fluor 488 goat anti-rabbit	Invitrogen	CAT# - A11034
Alexa Fluor 568 goat anti-rabbit	Invitrogen	CAT# - A11011
Alexa Fluor 568 goat anti-rat	Life	CAT# - A11077
Alexa Fluor 647 goat anti-Mouse	Life	CAT# - A21236
DyLight 550 anti-HA	Invitrogen	CAT# - 26183-D550
DyLight 488 anti-HA	Invitrogen	CAT# - 26183-D488
DyLight 550 anti-V5	Bio-rad	CAT# - Mca1360D550GA
DyLight 650 anti-V5	Invitrogen	CAT# - MA5-15253-D650

Living Colors DsRed Polyclonal Antibody	TakaraBio	CAT# - 632496

REAGENT or RESOURCE	SOURCE	IDENTIFIER
Experimental Models: Animal Genotypes		
smGFP reporter: *pJFRC200-10XUAS-IVS-myr::smGFP-HA (attP18), pJFRC216-13XLexAop2-IVS-myr::smGFP-V5 su(Hw)attP8.*	Nern et al., 2015	
UAS-Kir 2.1_1: *;pJFC49-10xUAS-IVS-eGFP Kir2.1 (Su(Hw)attP6);*	Michael Reiser and Ed Rogers, Janelia Farm Research Campus	
UAS-Kir 2.1_2: *;;pJFRC49-10xUAS-IVS-eGFP-Kir2.1 (attP2)*	Pfeiffer et al., 2012; von Reyn et al., 2014	
smGdP-STaR: *;LexAp-myr:tdTomato,UAS-R; Brp-RSR-SmGdP-V5-2A-LexA*	Peng et al., 2018	
myr:GFP: *pJFRC12-10XUAS-IVS-myr::GFP in su(Hw)attP1*	Pfeiffer et al.,2012	
LexAop-GFP: ***LexAop-GFP (attp8)***	Peng et al., 2018; Pfeiffer et al., 2012	
UAS-p35: 3rd chromosome	Pecot et al., 2014	
GRASP: *;LexAop-GFP_11/+; UAS-GFP_1-10/+*	Gordon & Scott, 2009	
UAS-CsChrimson: *UAS-CsChrimson-mVenus (attp18);;*	Klapoetke et al., 2014	
GF_1_LexA_: ;;*GF_1_LexA (attP2)*	Kennedy & Broadie, 2018	
GF_2_LexA: *;68A06_LexA (VK00022);*	Pfeiffer et al., 2010	
LC4_4-split-GAL4: ;*49C04_AD (attP2); 86D05_DBD (attP40)*	This paper	
LC4_1-split-GAL4: *;47H03_AD (attP40); 72E01_DBD (attP2)*	Wu et al., 2016	

LPLC1_1-split-GAL4 (OL0029B): ;*R64G09_P65ADZp (attp40);R37H05_ZpGbd (attP2)*	Wu et al., 2016	
LPLC1_2-split-GAL4 (SS02569): *;R64G09_P65ADZp (attP40); VT045990_ZpGbd (attP2)*	This paper	
LPLC1_3-split-GAL4 (SS02570): *R64G09_P65ADZp (attP40); VT063739_ZpGbd (attP2)*	This paper	
LPLC2-split-GAL4 (OL0048B): *;19G02_ P65ADZp (attp40);75G12_ ZpGbd (attP2)*	Wu et al., 2016	
LPLC2_LexA: *;75G12-LexAp65 (attP40)*;	Pfeiffer et al., 2010	

Acknowledgments

We thank members of the von Reyn lab for their critical reading and discussion of this manuscript. We would also like to thank Mark Dombrovskiy, a postdoctoral fellow in Larry Zipursky's lab at UCLA for recommending and sending *Drosophila* stocks. Funding was provided by the National Science Foundation Grant No. IOS-1921065 (CRvR) and the National Institutes of Health NINDS R01NS118562 (CRvR).

Competing interests

The authors declare no competing interests.

REFERENCES

Ache, J. M., Polsky, J., Alghailani, S., Parekh, R., Breads, P., Peek, M. Y., Bock, D. D., von Reyn, C. R., & Card, G. M. (2019). Neural Basis for Looming Size and Velocity Encoding in the Drosophila Giant Fiber Escape Pathway. *Current Biology*, *29*(6), 1073-1081.e4. https://doi.org/10.1016/j.cub.2019.01.079

Ackerman, S. D., Perez-Catalan, N. A., Freeman, M. R., & Doe, C. Q. (2021). Astrocytes close a motor circuit critical period. *Nature*, *592*(7854), 414–420. https://doi.org/10.1038/s41586-021-03441-2

Agathocleous, M., & Harris, W. A. (2009). From progenitors to differentiated cells in the vertebrate retina. *Annual Review of Cell and Developmental Biology*, *25*, 45–69. https://doi.org/10.1146/annurev.cellbio.042308.113259

Akin, O., Bajar, B. T., Keles, M. F., Frye, M. A., & Zipursky, S. L. (2019). Cell-type-Specific Patterned Stimulus-Independent Neuronal Activity in the Drosophila Visual System during Synapse Formation. *Neuron*, *101*(5), 894-904.e5. https://doi.org/10.1016/j.neuron.2019.01.008

Allen, M. J., Drummond, J. A., & Moffat, K. G. (1998). Development of the giant fiber neuron of Drosophila melanogaster. *Journal of Comparative Neurology*, *397*(4), 519–531. https://doi.org/10.1002/(SICI)1096-9861(19980810)397:4<519::AID-CNE5>3.0.CO;2-4

Allen, M. J., Godenschwege, T. A., Tanouye, M. A., & Phelan, P. (2006). Making an escape: Development and function of the Drosophila giant fibre system. *Seminars in Cell & Developmental Biology*, *17*(1), 31–41. https://doi.org/10.1016/j.semcdb.2005.11.011

Baines, R. A., Uhler, J. P., Thompson, A., Sweeney, S. T., & Bate, M. (2001a). Altered Electrical Properties in DrosophilaNeurons Developing without Synaptic Transmission.

Journal of Neuroscience, *21*(5), 1523–1531. https://doi.org/10.1523/JNEUROSCI.21-05-01523.2001

Baines, R. A., Uhler, J. P., Thompson, A., Sweeney, S. T., & Bate, M. (2001b). Altered Electrical Properties in DrosophilaNeurons Developing without Synaptic Transmission. *Journal of Neuroscience*, *21*(5), 1523–1531. https://doi.org/10.1523/JNEUROSCI.21-05-01523.2001

Bajar, B. T., Phi, N. T., Isaacman-Beck, J., Reichl, J., Randhawa, H., & Akin, O. (2022). A discrete neuronal population coordinates brain-wide developmental activity. *Nature*, *602*(7898), 639–646. https://doi.org/10.1038/s41586-022-04406-9

Batool, S., Raza, H., Zaidi, J., Riaz, S., Hasan, S., & Syed, N. I. (2019). Synapse formation: From cellular and molecular mechanisms to neurodevelopmental and neurodegenerative disorders. *Journal of Neurophysiology*, *121*(4), 1381–1397. https://doi.org/10.1152/jn.00833.2018

Berdnik, D., Chihara, T., Couto, A., & Luo, L. (2006). Wiring Stability of the Adult Drosophila Olfactory Circuit after Lesion. *Journal of Neuroscience*, *26*(13), 3367–3376. https://doi.org/10.1523/JNEUROSCI.4941-05.2006

Bollmann, J. H. (2019). The Zebrafish Visual System: From Circuits to Behavior. *Annual Review of Vision Science*, *5*, 269–293. https://doi.org/10.1146/annurev-vision-091718-014723

Bortner, C. D., & Cidlowski, J. A. (2020). Ions, the Movement of Water and the Apoptotic Volume Decrease. *Frontiers in Cell and Developmental Biology*, *8*. https://doi.org/10.3389/fcell.2020.611211

Brady, J., Vasin, A., & Bykhovskaia, M. (2021). The Accessory Helix of Complexin Stabilizes a Partially Unzippered State of the SNARE Complex and Mediates the Complexin Clamping Function In Vivo. *ENeuro*, *8*(2). https://doi.org/10.1523/ENEURO.0526-20.2021

Buddell, T., Friedman, V., Drozd, C. J., & Quinn, C. C. (2019). An autism-causing calcium channel variant functions with selective autophagy to alter axon targeting and behavior. *PLoS Genetics*, *15*(12), e1008488. https://doi.org/10.1371/journal.pgen.1008488

Cang, J., Savier, E., Barchini, J., & Liu, X. (2018). Visual Function, Organization, and Development of the Mouse Superior Colliculus. *Annual Review of Vision Science*, *4*(1), 239–262. https://doi.org/10.1146/annurev-vision-091517-034142

Carroll, B. J., Bertram, R., & Hyson, R. L. (2018). Intrinsic physiology of inhibitory neurons changes over auditory development. *Journal of Neurophysiology*, *119*(1), 290–304. https://doi.org/10.1152/jn.00447.2017

Chameau, P., Lucas, P., Melliti, K., Bournaud, R., & Shimahara, T. (1999). Development of multiple calcium channel types in cultured mouse hippocampal neurons. *Neuroscience*, *90*(2), 383–388. https://doi.org/10.1016/s0306-4522(98)00457-6

Chen, Y., Akin, O., Nern, A., Tsui, CY. K., Pecot, M. Y., & Zipursky, S. L. (2014). Cell-type Specific Labeling of Synapses in vivo through Synaptic Tagging with Recombination (STaR). *Neuron*, *81*(2), 280–293. https://doi.org/10.1016/j.neuron.2013.12.021

Cho, R. W., Song, Y., & Littleton, J. T. (2010). Comparative analysis of Drosophila and mammalian complexins as fusion clamps and facilitators of neurotransmitter release. *Molecular and Cellular Neurosciences*, *45*(4), 389–397. https://doi.org/10.1016/j.mcn.2010.07.012

Choi, B., Chen, Y.-C., & Desplan, C. (2021). Building a circuit through correlated spontaneous neuronal activity in the developing vertebrate and invertebrate visual systems. *Genes & Development*, *35*. https://doi.org/10.1101/gad.348241.121

Chowdhury, D., Watters, K., & Biederer, T. (2021). Synaptic recognition molecules in development and disease. *Current Topics in Developmental Biology*, *142*, 319–370. https://doi.org/10.1016/bs.ctdb.2020.12.009

Clements, J., Dolafi, T., Umayam, L., Neubarth, N. L., Berg, S., Scheffer, L. K., & Plaza, S. M. (2020). *neuPrint: Analysis Tools for EM Connectomics* (p. 2020.01.16.909465). bioRxiv. https://doi.org/10.1101/2020.01.16.909465

Courgeon, M., & Desplan, C. (2019). Coordination of neural patterning in the Drosophila visual system. *Current Opinion in Neurobiology*, *56*, 153–159. https://doi.org/10.1016/j.conb.2019.01.024

Crépel, V., Aronov, D., Jorquera, I., Represa, A., Ben-Ari, Y., & Cossart, R. (2007). A Parturition-Associated Nonsynaptic Coherent Activity Pattern in the Developing Hippocampus. *Neuron*, *54*(1), 105–120. https://doi.org/10.1016/j.neuron.2007.03.007

Davis, F. P., Nern, A., Picard, S., Reiser, M. B., Rubin, G. M., Eddy, S. R., & Henry, G. L. (2020). A genetic, genomic, and computational resource for exploring neural circuit function. *ELife*, *9*. https://doi.org/10.7554/eLife.50901

Dhande, O. S., Stafford, B. K., Lim, J.-H. A., & Huberman, A. D. (2015). Contributions of Retinal Ganglion Cells to Subcortical Visual Processing and Behaviors. *Annual Review of Vision Science*, *1*, 291–328. https://doi.org/10.1146/annurev-vision-082114-035502

D'Souza, S., & Lang, R. A. (2020). Retinal ganglion cell interactions shape the developing mammalian visual system. *Development (Cambridge, England)*, *147*(23), dev196535. https://doi.org/10.1242/dev.196535

Faust, T. E., Gunner, G., & Schafer, D. P. (2021). Mechanisms governing activity-dependent synaptic pruning in the developing mammalian CNS. *Nature Reviews Neuroscience*, *22*(11), 657–673. https://doi.org/10.1038/s41583-021-00507-y

Fayyazuddin, A., Zaheer, M. A., Hiesinger, P. R., & Bellen, H. J. (2006). The Nicotinic Acetylcholine Receptor Dα7 Is Required for an Escape Behavior inDrosophila. *PLoS Biology*, *4*(3), e63. https://doi.org/10.1371/journal.pbio.0040063

Feinberg, E. H., VanHoven, M. K., Bendesky, A., Wang, G., Fetter, R. D., Shen, K., & Bargmann, C. I. (2008). GFP Reconstitution Across Synaptic Partners (GRASP) Defines Cell Contacts and Synapses in Living Nervous Systems. *Neuron*, *57*(3), 353–363. https://doi.org/10.1016/j.neuron.2007.11.030

Ferreira, J. S., Dupuis, J. P., Kellermayer, B., Bénac, N., Manso, C., Bouchet, D., Levet, F., Butler, C., Sibarita, J.-B., & Groc, L. (2020). Distance-dependent regulation of NMDAR nanoscale organization along hippocampal neuron dendrites. *Proceedings of the National Academy of Sciences of the United States of America*, *117*(39), 24526–24533. https://doi.org/10.1073/pnas.1922477117

Fuerst, P. G., Koizumi, A., Masland, R. H., & Burgess, R. W. (2008). Neurite arborization and mosaic spacing in the mouse retina require DSCAM. *Nature*, *451*(7177), 470–474. https://doi.org/10.1038/nature06514

Gabbiani, F., Krapp, H. G., & Laurent, G. (1999). Computation of Object Approach by a Wide-Field, Motion-Sensitive Neuron. *The Journal of Neuroscience*, *19*(3), 1122–1141. https://doi.org/10.1523/JNEUROSCI.19-03-01122.1999

Gidon, A., & Segev, I. (2012). Principles Governing the Operation of Synaptic Inhibition in Dendrites. *Neuron*, *75*(2), 330–341. https://doi.org/10.1016/j.neuron.2012.05.015

Godenschwege, T. A., Hu, H., Shan-Crofts, X., Goodman, C. S., & Murphey, R. K. (2002). Bi-directional signaling by Semaphorin 1a during central synapse formation in Drosophila. *Nature Neuroscience*, *5*(12), 1294–1301. https://doi.org/10.1038/nn976

Goodman, D. P., Eldredge, A., & von Reyn, C. R. (2018). A novel assay to evaluate action selection in escape behavior. *Journal of Neuroscience Methods*, *304*, 154–161. https://doi.org/10.1016/j.jneumeth.2018.04.019

Gordon, M. D., & Scott, K. (2009). Motor control in a Drosophila taste circuit. *Neuron*, *61*(3), 373–384. https://doi.org/10.1016/j.neuron.2008.12.033

Gouwens, N. W., & Wilson, R. I. (2009). Signal propagation in Drosophila central neurons. *The Journal of Neuroscience: The Official Journal of the Society for Neuroscience*, *29*(19), 6239–6249. https://doi.org/10.1523/JNEUROSCI.0764-09.2009

Hill, J. J. (2012). *Target Recognition and Competitive Synaptogenesis in the Drosophila Giant Fiber System*. 139.

Holguera, I., & Desplan, C. (2018). Neuronal specification in space and time. *Science (New York, N.Y.)*, *362*(6411), 176–180. https://doi.org/10.1126/science.aas9435

Hong, W., Mosca, T. J., & Luo, L. (2012). Teneurins instruct synaptic partner matching in an olfactory map. *Nature*, *484*(7393), 201–207. https://doi.org/10.1038/nature10926

Hsu, C. T., & Bhandawat, V. (2016). Organization of descending neurons in Drosophila melanogaster. *Scientific Reports*, *6*, 20259. https://doi.org/10.1038/srep20259

Jacobs, K., Todman, M. G., Allen, M. J., Davies, J. A., & Bacon, J. P. (2000). Synaptogenesis in the giant-fibre system of Drosophila: Interaction of the giant fibre and its major motorneuronal target. *Development (Cambridge, England)*, *127*(23), 5203–5212.

Jang, H., Goodman, D. P., & Reyn, C. R. von. (2022). *Directional invariance in the Drosophila giant fiber escape circuit* (p. 2022.07.15.500271). bioRxiv. https://doi.org/10.1101/2022.07.15.500271

Jefferis, G. S. X. E., Vyas, R. M., Berdnik, D., Ramaekers, A., Stocker, R. F., Tanaka, N. K., Ito, K., & Luo, L. (2004). Developmental origin of wiring specificity in the olfactory system of Drosophila. *Development (Cambridge, England)*, *131*(1), 117–130. https://doi.org/10.1242/dev.00896

Keck, T., Toyoizumi, T., Chen, L., Doiron, B., Feldman, D. E., Fox, K., Gerstner, W., Haydon, P. G., Hübener, M., Lee, H.-K., Lisman, J. E., Rose, T., Sengpiel, F., Stellwagen, D., Stryker, M. P., Turrigiano, G. G., & van Rossum, M. C. (2017). Integrating Hebbian and homeostatic plasticity: The current state of the field and future research directions. *Philosophical Transactions of the Royal Society B: Biological Sciences*, *372*(1715), 20160158. https://doi.org/10.1098/rstb.2016.0158

Keleş, M., & Frye, M. A. (2017). The eyes have it. *ELife*, *6*, e24896. https://doi.org/10.7554/eLife.24896

Kennedy, T., & Broadie, K. (2018). Newly Identified Electrically Coupled Neurons Support Development of the Drosophila Giant Fiber Model Circuit. *ENeuro*, *5*(6). https://doi.org/10.1523/ENEURO.0346-18.2018

Kim, U. S., Mahroo, O. A., Mollon, J. D., & Yu-Wai-Man, P. (2021). Retinal Ganglion Cells—Diversity of Cell Types and Clinical Relevance. *Frontiers in Neurology*, *12*. https://www.frontiersin.org/article/10.3389/fneur.2021.661938

Kirkby, L. A., Sack, G. S., Firl, A., & Feller, M. B. (2013). A Role for Correlated Spontaneous Activity in the Assembly of Neural Circuits. *Neuron*, *80*(5), 1129–1144. https://doi.org/10.1016/j.neuron.2013.10.030

Klapoetke, N. C., Murata, Y., Kim, S. S., Pulver, S. R., Birdsey-Benson, A., Cho, Y. K., Morimoto, T. K., Chuong, A. S., Carpenter, E. J., Tian, Z., Wang, J., Xie, Y., Yan, Z., Zhang, Y., Chow, B. Y., Surek, B., Melkonian, M., Jayaraman, V., Constantine-Paton, M., … Boyden, E. S. (2014). Independent optical excitation of distinct neural populations. *Nature Methods*, *11*(3), 338–346. https://doi.org/10.1038/nmeth.2836

Klapoetke, N. C., Nern, A., Peek, M. Y., Rogers, E. M., Breads, P., Rubin, G. M., Reiser, M. B., & Card, G. M. (2017). Ultra-selective looming detection from radial motion opponency. *Nature*, *551*(7679), 237–241. https://doi.org/10.1038/nature24626

Klapoetke, N. C., Nern, A., Rogers, E. M., Rubin, G. M., Reiser, M. B., & Card, G. M. (2022). A functionally ordered visual feature map in the Drosophila brain. *Neuron*, S0896-6273(22)00178-7. https://doi.org/10.1016/j.neuron.2022.02.013

Knapek, S., Sigrist, S., & Tanimoto, H. (2011). Bruchpilot, a synaptic active zone protein for anesthesia-resistant memory. *The Journal of Neuroscience: The Official Journal of the Society for Neuroscience*, *31*(9), 3453–3458. https://doi.org/10.1523/JNEUROSCI.2585-10.2011

Kolodkin, A. L., & Hiesinger, P. R. (2017). Wiring visual systems: Common and divergent mechanisms and principles. *Current Opinion in Neurobiology*, *42*, 128–135. https://doi.org/10.1016/j.conb.2016.12.006

Kondratskyi, A., Kondratska, K., Skryma, R., & Prevarskaya, N. (2015). Ion channels in the regulation of apoptosis. *Biochimica et Biophysica Acta (BBA) - Biomembranes*, *1848*(10, Part B), 2532–2546. https://doi.org/10.1016/j.bbamem.2014.10.030

Kurmangaliyev, Y. Z., Yoo, J., Valdes-Aleman, J., Sanfilippo, P., & Zipursky, S. L. (2020). Transcriptional Programs of Circuit Assembly in the Drosophila Visual System. *Neuron*, *108*(6), 1045-1057.e6. https://doi.org/10.1016/j.neuron.2020.10.006

Kutsarova, E., Munz, M., & Ruthazer, E. S. (2017). Rules for Shaping Neural Connections in the Developing Brain. *Frontiers in Neural Circuits*, *10*. https://doi.org/10.3389/fncir.2016.00111

Lawrence Zipursky, S., & Grueber, W. B. (2013). The Molecular Basis of Self-Avoidance. *Annual Review of Neuroscience*, *36*(1), 547–568. https://doi.org/10.1146/annurev-neuro-062111-150414

Lefebvre, J. L., Kostadinov, D., Chen, W. V., Maniatis, T., & Sanes, J. R. (2012). Protocadherins mediate dendritic self-avoidance in the mammalian nervous system. *Nature*, *488*(7412), 517–521. https://doi.org/10.1038/nature11305

Lefebvre, J. L., Sanes, J. R., & Kay, J. N. (2015). Development of Dendritic Form and Function. *Annual Review of Cell and Developmental Biology*, *31*(1), 741–777. https://doi.org/10.1146/annurev-cellbio-100913-013020

Li, T., Fu, T.-M., Wong, K. K. L., Li, H., Xie, Q., Luginbuhl, D. J., Wagner, M. J., Betzig, E., & Luo, L. (2021). Cellular bases of olfactory circuit assembly revealed by systematic time-lapse imaging. *Cell*, *184*(20), 5107-5121.e14. https://doi.org/10.1016/j.cell.2021.08.030

Li, X., Erclik, T., Bertet, C., Chen, Z., Voutev, R., Venkatesh, S., Morante, J., Celik, A., & Desplan, C. (2013). Temporal patterning of Drosophila medulla neuroblasts controls neural fates. *Nature*, *498*(7455), 456–462. https://doi.org/10.1038/nature12319

Liu, C., Trush, O., Han, X., Wang, M., Takayama, R., Yasugi, T., Hayashi, T., & Sato, M. (2020). Dscam1 establishes the columnar units through lineage-dependent repulsion between sister neurons in the fly brain. *Nature Communications*, *11*(1), 4067. https://doi.org/10.1038/s41467-020-17931-w

Louis, M., & Simpson, J. H. (2018). Disentangling the strings that organize behavior. *ELife*, *7*, e38410. https://doi.org/10.7554/eLife.38410

Luhmann, H. J., & Khazipov, R. (2018). Neuronal Activity Patterns in the Developing Barrel Cortex. *Neuroscience*, *368*, 256–267. https://doi.org/10.1016/j.neuroscience.2017.05.025

Malmersjö, S., Rebellato, P., Smedler, E., Planert, H., Kanatani, S., Liste, I., Nanou, E., Sunner, H., Abdelhady, S., Zhang, S., Andäng, M., El Manira, A., Silberberg, G., Arenas, E., & Uhlén, P. (2013). Neural progenitors organize in small-world networks to promote cell proliferation. *Proceedings of the National Academy of Sciences*, *110*(16), E1524–E1532. https://doi.org/10.1073/pnas.1220179110

Mayseless, O., Berns, D. S., Yu, X. M., Riemensperger, T., Fiala, A., & Schuldiner, O. (2018). Developmental Coordination during Olfactory Circuit Remodeling in Drosophila. *Neuron*, *99*(6), 1204-1215.e5. https://doi.org/10.1016/j.neuron.2018.07.050

Megighian, A., Zordan, M., Pantano, S., Scorzeto, M., Rigoni, M., Zanini, D., Rossetto, O., & Montecucco, C. (2013). Evidence for a radial SNARE super-complex mediating neurotransmitter release at the Drosophila neuromuscular junction. *Journal of Cell Science*, *126*(14), 3134–3140. https://doi.org/10.1242/jcs.123802

Mensh, B., & Kording, K. (2017). Ten simple rules for structuring papers. *PLOS Computational Biology*, *13*(9), e1005619. https://doi.org/10.1371/journal.pcbi.1005619

Millard, S. S., Flanagan, J. J., Pappu, K. S., Wu, W., & Zipursky, S. L. (2007). Dscam2 mediates axonal tiling in the Drosophila visual system. *Nature*, *447*(7145), 720–724. https://doi.org/10.1038/nature05855

Mishchenko, Y., Hu, T., Spacek, J., Mendenhall, J., Harris, K. M., & Chklovskii, D. B. (2010). Ultrastructural analysis of hippocampal neuropil from the connectomics perspective. *Neuron*, *67*(6), 1009–1020. https://doi.org/10.1016/j.neuron.2010.08.014

Mora, N., Oliva, C., Fiers, M., Ejsmont, R., Soldano, A., Zhang, T.-T., Yan, J., Claeys, A., De Geest, N., & Hassan, B. A. (2018). A Temporal Transcriptional Switch Governs Stem Cell Division, Neuronal Numbers, and Maintenance of Differentiation. *Developmental Cell*, *45*(1), 53-66.e5. https://doi.org/10.1016/j.devcel.2018.02.023

Moreno-Juan, V., Filipchuk, A., Antón-Bolaños, N., Mezzera, C., Gezelius, H., Andrés, B., Rodríguez-Malmierca, L., Susín, R., Schaad, O., Iwasato, T., Schüle, R., Rutlin, M., Nelson, S., Ducret, S., Valdeolmillos, M., Rijli, F. M., & López-Bendito, G. (2017). Prenatal thalamic waves regulate cortical area size prior to sensory processing. *Nature Communications*, *8*(1), 14172. https://doi.org/10.1038/ncomms14172

Morimoto, M. M., Nern, A., Zhao, A., Rogers, E. M., Wong, A. M., Isaacson, M. D., Bock, D. D., Rubin, G. M., & Reiser, M. B. (2020). Spatial readout of visual looming in the central brain of Drosophila. *ELife*, *9*, e57685. https://doi.org/10.7554/eLife.57685

Moruzzi, A. M., Abedini, N. C., Hansen, M. A., Olson, J. E., & Bosma, M. M. (2009). Differential expression of membrane conductances underlies spontaneous event initiation by rostral midline neurons in the embryonic mouse hindbrain. *The Journal of Physiology*, *587*(21), 5081–5093. https://doi.org/10.1113/jphysiol.2009.180091

Murphey, R. K., Froggett, S. J., Caruccio, P., Shan-Crofts, X., Kitamoto, T., & Godenschwege, T. A. (2003). Targeted expression of shibire ts and semaphorin 1a reveals critical periods for synapse formation in the giant fiber of Drosophila. *Development (Cambridge, England)*, *130*(16), 3671–3682.

Nakashima, A., Ihara, N., Shigeta, M., Kiyonari, H., Ikegaya, Y., & Takeuchi, H. (2019). Structured spike series specify gene expression patterns for olfactory circuit formation. *Science (New York, N.Y.)*, *365*(6448), eaaw5030. https://doi.org/10.1126/science.aaw5030

Namiki, S., Dickinson, M. H., Wong, A. M., Korff, W., & Card, G. M. (2018). The functional organization of descending sensory-motor pathways in Drosophila. *ELife*, *7*, e34272. https://doi.org/10.7554/eLife.34272

Nern, A., Pfeiffer, B. D., & Rubin, G. M. (2015). Optimized tools for multicolor stochastic labeling reveal diverse stereotyped cell arrangements in the fly visual system. *Proceedings of the National Academy of Sciences*, *112*(22), E2967–E2976. https://doi.org/10.1073/pnas.1506763112

Nern, A., Zhu, Y., & Zipursky, S. L. (2008). Local N-Cadherin Interactions Mediate Distinct Steps in the Targeting of Lamina Neurons. *Neuron*, *58*(1), 34–41. https://doi.org/10.1016/j.neuron.2008.03.022

Niven, J. E., Vähäsöyrinki, M., Kauranen, M., Hardie, R. C., Juusola, M., & Weckström, M. (2003). The contribution of Shaker K+ channels to the information capacity of Drosophila photoreceptors. *Nature*, *421*(6923), 630–634. https://doi.org/10.1038/nature01384

Özel, M. N., Simon, F., Jafari, S., Holguera, I., Chen, Y.-C., Benhra, N., El-Danaf, R. N., Kapuralin, K., Malin, J. A., Konstantinides, N., & Desplan, C. (2021). Neuronal diversity and convergence in a visual system developmental atlas. *Nature*, *589*(7840), 88–95. https://doi.org/10.1038/s41586-020-2879-3

Pan, Y., & Monje, M. (2020). Activity Shapes Neural Circuit Form and Function: A Historical Perspective. *The Journal of Neuroscience: The Official Journal of the Society for Neuroscience*, *40*(5), 944–954. https://doi.org/10.1523/JNEUROSCI.0740-19.2019

Pecot, M. Y., Chen, Y., Akin, O., Chen, Z., Tsui, C. Y. K., & Zipursky, S. L. (2014). Sequential Axon-Derived Signals Couple Target Survival and Layer Specificity in the Drosophila Visual System. *Neuron*, *82*(2), 320–333. https://doi.org/10.1016/j.neuron.2014.02.045

Peek, M. Y. (2018). *Control of Escape Behavior by Descending Neurons in Drosophila Melanogaster* [ProQuest Dissertations Publishing]. https://www.proquest.com/docview/2162562914/294D136122F84F88PQ/2

Peng, J., Santiago, I. J., Ahn, C., Gur, B., Tsui, C. K., Su, Z., Xu, C., Karakhanyan, A., Silies, M., & Pecot, M. Y. (2018). Drosophila Fezf coordinates laminar-specific connectivity through cell-intrinsic and cell-extrinsic mechanisms. *ELife*, *7*, e33962. https://doi.org/10.7554/eLife.33962

Pézier, A. P., Jezzini, S. H., Bacon, J. P., & Blagburn, J. M. (2016). Shaking B Mediates Synaptic Coupling between Auditory Sensory Neurons and the Giant Fiber of Drosophila melanogaster. *PloS One*, *11*(4), e0152211. https://doi.org/10.1371/journal.pone.0152211

Pfeiffer, B. D., Ngo, T.-T. B., Hibbard, K. L., Murphy, C., Jenett, A., Truman, J. W., & Rubin, G. M. (2010). Refinement of Tools for Targeted Gene Expression in Drosophila. *Genetics*, *186*(2), 735–755. https://doi.org/10.1534/genetics.110.119917

Pfeiffer, B. D., Truman, J. W., & Rubin, G. M. (2012). Using translational enhancers to increase transgene expression in Drosophila. *Proceedings of the National Academy of Sciences of the United States of America*, *109*(17), 6626–6631. https://doi.org/10.1073/pnas.1204520109

Phelan, P., Goulding, L. A., Tam, J. L. Y., Allen, M. J., Dawber, R. J., Davies, J. A., & Bacon, J. P. (2008). Molecular mechanism of rectification at identified electrical synapses in the Drosophila giant fiber system. *Current Biology: CB*, *18*(24), 1955–1960. https://doi.org/10.1016/j.cub.2008.10.067

Phelan, P., Nakagawa, M., Wilkin, M., Moffat, K., O'Kane, C., Davies, J., & Bacon, J. (1996). Mutations in shaking-B prevent electrical synapse formation in the Drosophila giant fiber system. *The Journal of Neuroscience*, *16*(3), 1101–1113. https://doi.org/10.1523/JNEUROSCI.16-03-01101.1996

Pinto-Teixeira, F., Koo, C., Rossi, A. M., Neriec, N., Bertet, C., Li, X., Del-Valle-Rodriguez, A., & Desplan, C. (2018). Development of Concurrent Retinotopic Maps in the Fly Motion Detection Circuit. *Cell*, *173*(2), 485-498.e11. https://doi.org/10.1016/j.cell.2018.02.053

Puñal, V. M., Ahmed, M., Thornton-Kolbe, E. M., & Clowney, E. J. (2021). Untangling the wires: Development of sparse, distributed connectivity in the mushroom body calyx. *Cell and Tissue Research*, *383*(1), 91–112. https://doi.org/10.1007/s00441-020-03386-4

Rees, C. L., Moradi, K., & Ascoli, G. A. (2017). Weighing the Evidence in Peters' Rule: Does Neuronal Morphology Predict Connectivity? *Trends in Neurosciences*, *40*(2), 63–71. https://doi.org/10.1016/j.tins.2016.11.007

Reyn, C. R. von, Nern, A., Williamson, W. R., Breads, P., Wu, M., Namiki, S., & Card, G. M. (2017). Feature Integration Drives Probabilistic Behavior in the Drosophila Escape Response. *Neuron*, *94*(6), 1190-1204.e6. https://doi.org/10.1016/j.neuron.2017.05.036

Rheaume, B. A., Jereen, A., Bolisetty, M., Sajid, M. S., Yang, Y., Renna, K., Sun, L., Robson, P., & Trakhtenberg, E. F. (2018). Single cell transcriptome profiling of retinal ganglion cells identifies cellular subtypes. *Nature Communications*, *9*(1), 2759. https://doi.org/10.1038/s41467-018-05134-3

Ribeiro, I. M. A., Drews, M., Bahl, A., Machacek, C., Borst, A., & Dickson, B. J. (2018). Visual Projection Neurons Mediating Directed Courtship in Drosophila. *Cell*, *174*(3), 607-621.e18. https://doi.org/10.1016/j.cell.2018.06.020

Sakuma, C., Anzo, M., Miura, M., & Chihara, T. (2014). Development of olfactory projection neuron dendrites that contribute to wiring specificity of the *Drosophila* olfactory circuit. *Genes & Genetic Systems*, *89*(1), 17–26. https://doi.org/10.1266/ggs.89.17

Sanes, J. R., & Zipursky, S. L. (2010). Design principles of insect and vertebrate visual systems. *Neuron*, *66*(1), 15–36. https://doi.org/10.1016/j.neuron.2010.01.018

Sanes, J. R., & Zipursky, S. L. (2020). Synaptic Specificity, Recognition Molecules, and Assembly of Neural Circuits. *Cell*, *181*(3), 536–556. https://doi.org/10.1016/j.cell.2020.04.008

Sassoè-Pognetto, M., & Patrizi, A. (2017). The Purkinje cell as a model of synaptogenesis and synaptic specificity. *Brain Research Bulletin*, *129*, 12–17. https://doi.org/10.1016/j.brainresbull.2016.10.004

Scheffer, L. K., Xu, C. S., Januszewski, M., Lu, Z., Takemura, S.-Y., Hayworth, K. J., Huang, G. B., Shinomiya, K., Maitlin-Shepard, J., Berg, S., Clements, J., Hubbard, P. M., Katz, W. T., Umayam, L., Zhao, T., Ackerman, D., Blakely, T., Bogovic, J., Dolafi, T., … Plaza, S. M. (2020a). A connectome and analysis of the adult Drosophila central brain. *ELife*, *9*, e57443. https://doi.org/10.7554/eLife.57443

Scheffer, L. K., Xu, C. S., Januszewski, M., Lu, Z., Takemura, S.-Y., Hayworth, K. J., Huang, G. B., Shinomiya, K., Maitlin-Shepard, J., Berg, S., Clements, J., Hubbard, P. M., Katz, W. T., Umayam, L., Zhao, T., Ackerman, D., Blakely, T., Bogovic, J., Dolafi, T., … Plaza, S. M. (2020b). A connectome and analysis of the adult Drosophila central brain. *ELife*, *9*, e57443. https://doi.org/10.7554/eLife.57443

Schilling, T., Ali, A. H., Leonhardt, A., Borst, A., & Pujol-Martí, J. (2019). Transcriptional control of morphological properties of direction-selective T4/T5 neurons in Drosophila. *Development*, *146*(2). https://doi.org/10.1242/dev.169763

Schmucker, D., Clemens, J. C., Shu, H., Worby, C. A., Xiao, J., Muda, M., Dixon, J. E., & Zipursky, S. L. (2000). Drosophila Dscam Is an Axon Guidance Receptor Exhibiting Extraordinary Molecular Diversity. *Cell*, *101*(6), 671–684. https://doi.org/10.1016/S0092-8674(00)80878-8

Scholz, N., Ehmann, N., Sachidanandan, D., Imig, C., Cooper, B. H., Jahn, O., Reim, K., Brose, N., Meyer, J., Lamberty, M., Altrichter, S., Bormann, A., Hallermann, S., Pauli, M., Heckmann, M., Stigloher, C., Langenhan, T., & Kittel, R. J. (2019). Complexin cooperates

with Bruchpilot to tether synaptic vesicles to the active zone cytomatrix. *The Journal of Cell Biology*, *218*(3), 1011–1026. https://doi.org/10.1083/jcb.201806155

Singh, A. P., VijayRaghavan, K., & Rodrigues, V. (2010). Dendritic refinement of an identified neuron in the Drosophila CNS is regulated by neuronal activity and Wnt signaling. *Development (Cambridge, England)*, *137*(8), 1351–1360. https://doi.org/10.1242/dev.044131

Smedler, E., Louhivuori, L., Romanov, R. A., Masini, D., Dehnisch Ellström, I., Wang, C., Caramia, M., West, Z., Zhang, S., Rebellato, P., Malmersjö, S., Brusini, I., Kanatani, S., Fisone, G., Harkany, T., & Uhlén, P. (2022). Disrupted Cacna1c gene expression perturbs spontaneous Ca2+ activity causing abnormal brain development and increased anxiety. *Proceedings of the National Academy of Sciences*, *119*(7), e2108768119. https://doi.org/10.1073/pnas.2108768119

Spruston, N. (2008). Pyramidal neurons: Dendritic structure and synaptic integration. *Nature Reviews Neuroscience*, *9*(3), 206–221. https://doi.org/10.1038/nrn2286

Strausfeld, N. J., Sinakevitch, I., & Okamura, J.-Y. (2007). Organization of local interneurons in optic glomeruli of the dipterous visual system and comparisons with the antennal lobes. *Developmental Neurobiology*, *67*(10), 1267–1288. https://doi.org/10.1002/dneu.20396

Strother, J. A., Wu, S.-T., Wong, A. M., Nern, A., Rogers, E. M., Le, J. Q., Rubin, G. M., & Reiser, M. B. (2017). The Emergence of Directional Selectivity in the Visual Motion Pathway of Drosophila. *Neuron*, *94*(1), 168-182.e10. https://doi.org/10.1016/j.neuron.2017.03.010

Su, Y., Shin, J., Zhong, C., Wang, S., Roychowdhury, P., Lim, J., Kim, D., Ming, G., & Song, H. (2017). Neuronal activity modifies the chromatin accessibility landscape in the adult brain. *Nature Neuroscience*, *20*(3), 476–483. https://doi.org/10.1038/nn.4494

Szabò, I., Leanza, L., Gulbins, E., & Zoratti, M. (2012). Physiology of potassium channels in the inner membrane of mitochondria. *Pflügers Archiv - European Journal of Physiology*, *463*(2), 231–246. https://doi.org/10.1007/s00424-011-1058-7

Tessier, C. R., & Broadie, K. (2009). Activity-dependent modulation of neural circuit synaptic connectivity. *Frontiers in Molecular Neuroscience*, *2*. https://doi.org/10.3389/neuro.02.008.2009

von Reyn, C. R., Breads, P., Peek, M. Y., Zheng, G. Z., Williamson, W. R., Yee, A. L., Leonardo, A., & Card, G. M. (2014). A spike-timing mechanism for action selection. *Nature Neuroscience*, *17*(7), 962–970. https://doi.org/10.1038/nn.3741

von Reyn, C. R., Nern, A., Williamson, W. R., Breads, P., Wu, M., Namiki, S., & Card, G. M. (2017). Feature Integration Drives Probabilistic Behavior in the Drosophila Escape Response. *Neuron*, *94*(6), 1190-1204.e6. https://doi.org/10.1016/j.neuron.2017.05.036

Vonhoff, F., & Keshishian, H. (2017). Activity-Dependent Synaptic Refinement: New Insights from Drosophila. *Frontiers in Systems Neuroscience*, *11*. https://doi.org/10.3389/fnsys.2017.00023

Wagh, D. A., Rasse, T. M., Asan, E., Hofbauer, A., Schwenkert, I., Dürrbeck, H., Buchner, S., Dabauvalle, M.-C., Schmidt, M., Qin, G., Wichmann, C., Kittel, R., Sigrist, S. J., & Buchner, E. (2006). Bruchpilot, a protein with homology to ELKS/CAST, is required for structural integrity and function of synaptic active zones in Drosophila. *Neuron*, *49*(6), 833–844. https://doi.org/10.1016/j.neuron.2006.02.008

West, A. E., & Greenberg, M. E. (2011). Neuronal Activity–Regulated Gene Transcription in Synapse Development and Cognitive Function. *Cold Spring Harbor Perspectives in Biology*, *3*(6), a005744. https://doi.org/10.1101/cshperspect.a005744

Wu, J. S., & Luo, L. (2006). A protocol for dissecting Drosophila melanogaster brains for live imaging or immunostaining. *Nature Protocols*, *1*(4), 2110–2115. https://doi.org/10.1038/nprot.2006.336

Wu, M., Nern, A., Williamson, W. R., Morimoto, M. M., Reiser, M. B., Card, G. M., & Rubin, G. M. (2016). Visual projection neurons in the Drosophila lobula link feature detection to distinct behavioral programs. *ELife*, *5*, e21022. https://doi.org/10.7554/eLife.21022

Xu, S., Xiao, Q., Cosmanescu, F., Sergeeva, A. P., Yoo, J., Lin, Y., Katsamba, P. S., Ahlsen, G., Kaufman, J., Linaval, N. T., Lee, P.-T., Bellen, H. J., Shapiro, L., Honig, B., Tan, L., & Zipursky, S. L. (2018). Interactions between the Ig-Superfamily Proteins DIP-α and Dpr6/10 Regulate Assembly of Neural Circuits. *Neuron*, *100*(6), 1369-1384.e6. https://doi.org/10.1016/j.neuron.2018.11.001

Yamagata, M., & Sanes, J. R. (2012). Transgenic strategy for identifying synaptic connections in mice by fluorescence complementation (GRASP). *Frontiers in Molecular Neuroscience*, *5*. https://doi.org/10.3389/fnmol.2012.00018

Yogev, S., & Shen, K. (2014). Cellular and Molecular Mechanisms of Synaptic Specificity. *Annual Review of Cell and Developmental Biology*, *30*(1), 417–437. https://doi.org/10.1146/annurev-cellbio-100913-012953

Zheng, Z., Lauritzen, J. S., Perlman, E., Robinson, C. G., Nichols, M., Milkie, D., Torrens, O., Price, J., Fisher, C. B., Sharifi, N., Calle-Schuler, S. A., Kmecova, L., Ali, I. J., Karsh, B., Trautman, E. T., Bogovic, J. A., Hanslovsky, P., Jefferis, G. S. X. E., Kazhdan, M., …

Bock, D. D. (2018). A Complete Electron Microscopy Volume of the Brain of Adult Drosophila melanogaster. *Cell*, *174*(3), 730-743.e22. https://doi.org/10.1016/j.cell.2018.06.019

Supplemental Figures

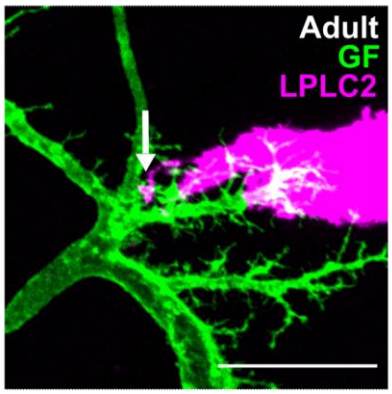

Figure 1-figure supplement 1. LPLC2 mistargeting onto GF. Confocal images of the adult GF (green) with respect to LPLC2 (magenta). A single LPLC2 axon extends into an abnormally medial position on the GF (arrow). Scale bar, 20μm.

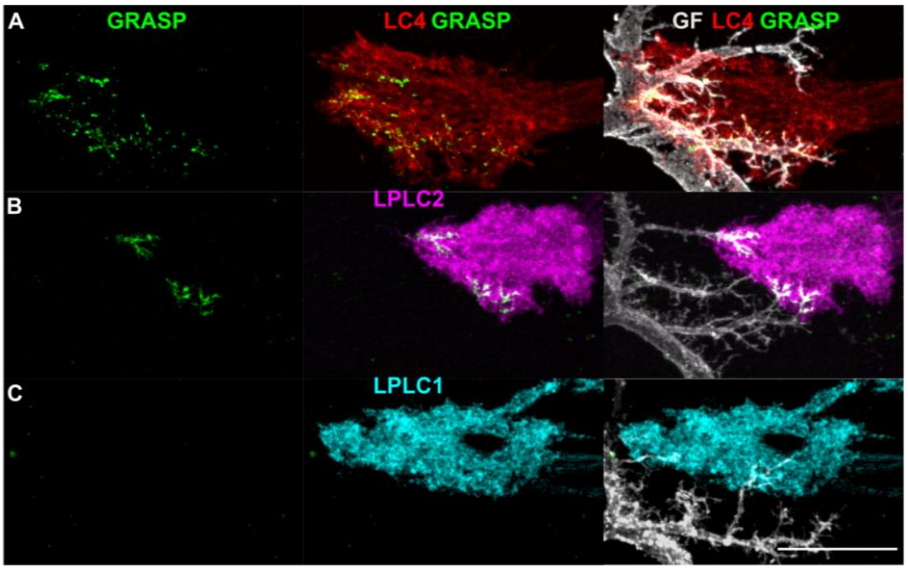

Figure 1-figure supplement 2. Expression of GRASP reveals putative contacts between neuronal membranes.
(A-C) (Left) Max intensity projection of reconstituted GFP signal (green) between GF and LC4 (A), LPLC2 (B) and LPLC1 (C). (Middle) Max intensity projections of LC axonal membranes and GRASP signal. (Right) Max intensity projections of LC axonal membranes with GRASP signal and GF (gray). Scale bar, 20μm.

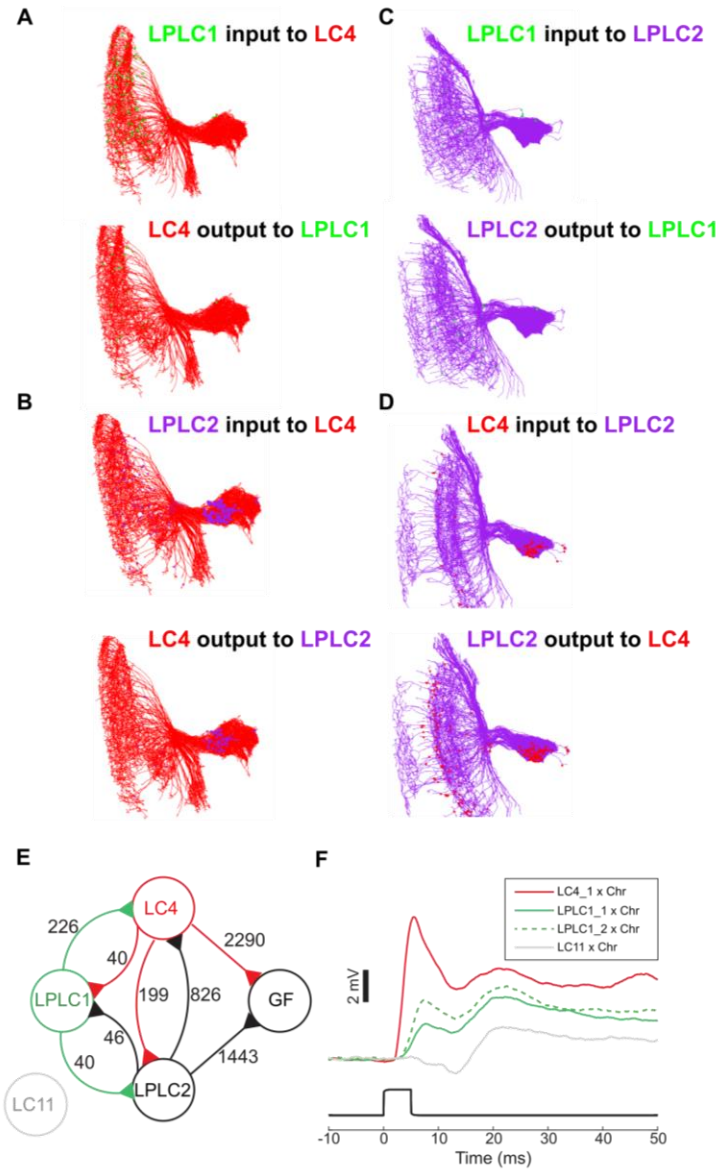

Figure 1-figure supplement 3. EM reconstruction of connections between select LC neurons reveal reciprocal connectivity.

(A,B) Adult LC4 (red) EM reconstruction with reciprocal synapses with LPLC1 (green) (A) and LPLC2 (purple) (B).

(C,D) Adult LPLC2 (purple) EM reconstruction with reciprocal synapses with LPLC1 (green) (C) and LC4 (red) (D).

(E) Circuit diagram of connections between GF and select LCs based on hemibrain dataset was used.

(F) LPLC1 activation (CsChrimson) leads to a delayed activation of GF, likely through indirect coupling observed in (E). Average GF responses following activation of LC4 (red), LPLC1 with two different driver lines (green solid and dashed), and LC11 (gray) a negative control that does not have direct connections with the GF or GF circuit LCs (N=3-8 flies).

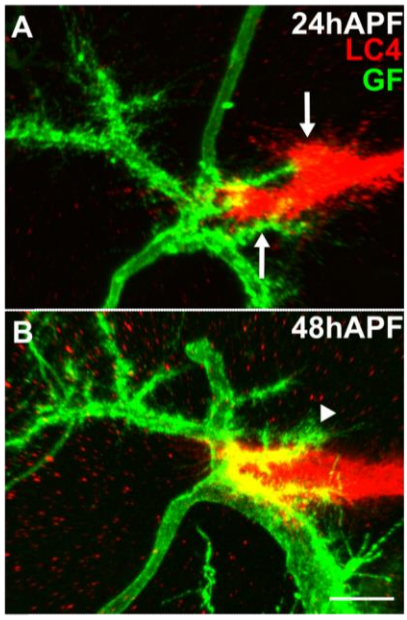

Figure 3 – figure supplement 1. Max intensity projection images of GF (green) and LC4 (red) at 24hAPF **(A),** and 48hAPF **(B).** Arrows pointing to dorsal (top) and ventral (bottom) aspects of LC4. Arrowhead indicates GF dendrite extending past LC4 axons. Scale bar, 20 μm.

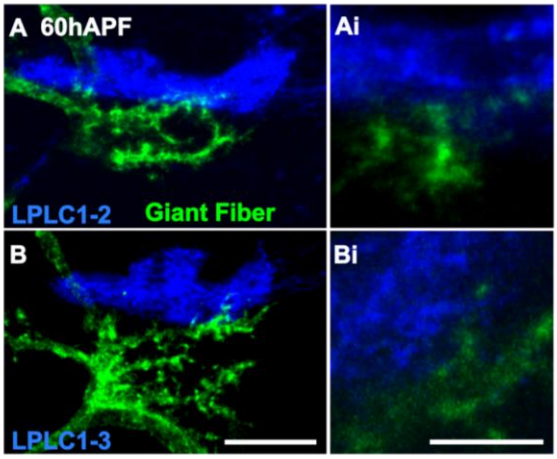

Figure 3 – figure supplement 2. LPLC1 is limited in its developmental interactions with GF. Max intensity projections of LPLC1-2 **(A)** and LPLC1-3 **(B)** driver lines with GF at 60hAPF. Scale bar, 20 µm. **(Ai,Bi)** Sub-stacks of 4 z-planes, showing GF and LPLC1 appositions with the LPLC1-2 and LPLC1-3 driver lines, respectively. Scale bar, 5µm N=2 half-brains.

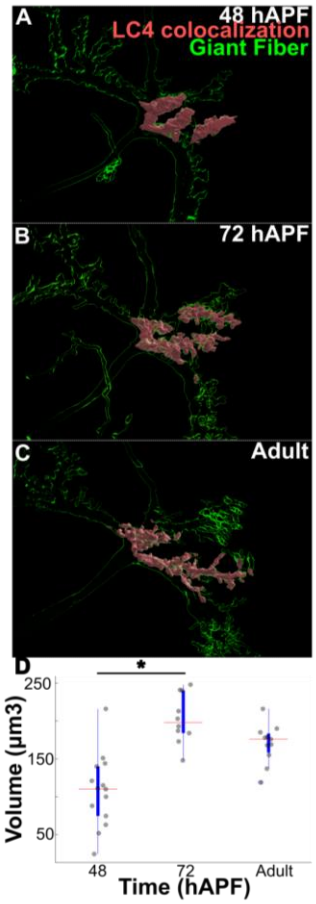

Figure 3 – figure supplement 3. Colocalization trends observed between GF and LC4 are replicated using Imaris Analysis Software

(**A-C**) 3D rendering of GF neurons (green) created in IMARIS with LC4 colocalized pixels (red) superimposed at distinct time points during metamorphosis.

(**D**) Quantification of colocalization between GF and LC4 in (A-C), an unpaired non-parametric Kruskal-Wallis test was performed ($p=1.06637 \times 10^{-5}$), followed by Dunn-Tukey-Kramer multiple comparison post hoc test, * $p<.05$. $N \geq 11$ half-brains per condition.

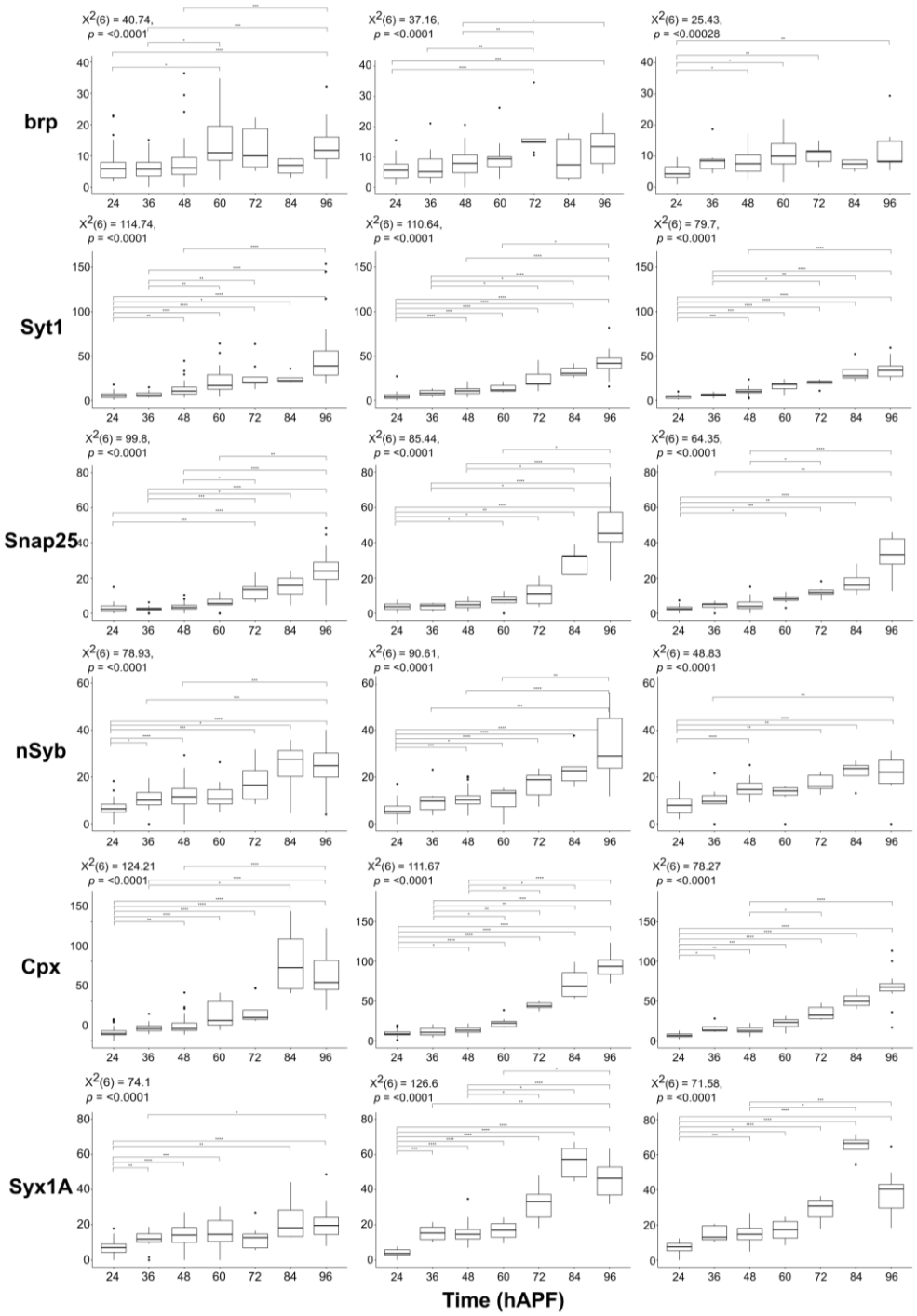
brp
Syt1
Snap25
nSyb
Cpx
Syx1A
X2(6) = 40.74, p = <0.0001
X2(6) = 37.16, p = <0.0001
X2(6) = 25.43, p = <0.00028
X2(6) = 114.74, p = <0.0001
X2(6) = 110.64, p = <0.0001
X2(6) = 79.7, p = <0.0001
X2(6) = 99.8, p = <0.0001
X2(6) = 85.44, p = <0.0001
X2(6) = 64.35, p = <0.0001
X2(6) = 78.93, p = <0.0001
X2(6) = 90.61, p = <0.0001
X2(6) = 48.83 p = <0.0001
X2(6) = 124.21 p = <0.0001
X2(6) = 111.67 p = <0.0001
X2(6) = 78.27 p = <0.0001
X2(6) = 74.1 p = <0.0001
X2(6) = 126.6 p = <0.0001
X2(6) = 71.58, p = <0.0001
24 36 48 60 72 84 96
Time (hAPF)

1329

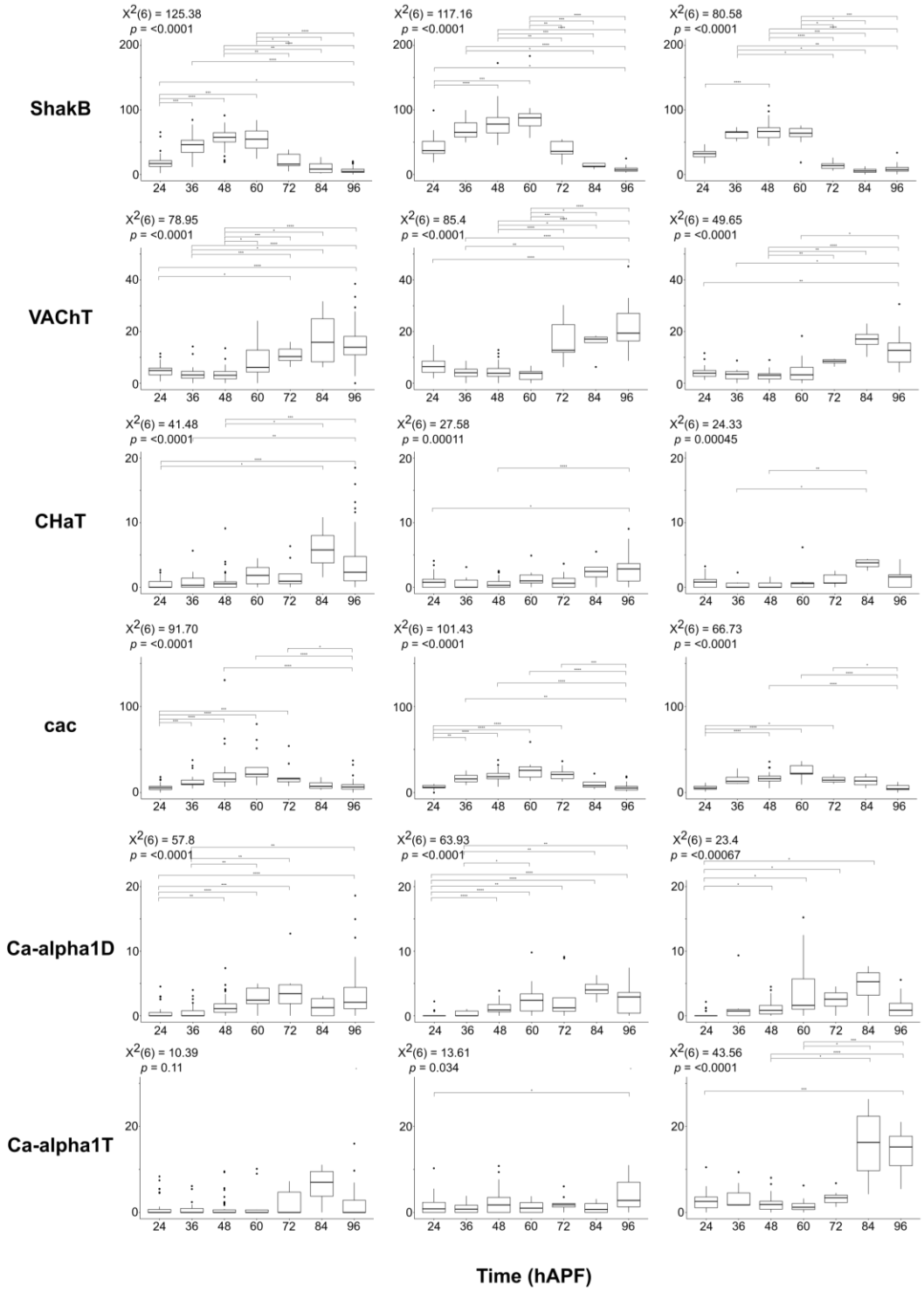
ShakB
VAChT
CHaT
cac
Ca-alpha1D
Ca-alpha1T
X2(6) = 125.38
p = <0.0001
X2(6) = 117.16
p = <0.0001
X2(6) = 80.58
p = <0.0001
X2(6) = 78.95
p = <0.0001
X2(6) = 85.4
p = <0.0001
X2(6) = 49.65
p = <0.0001
X2(6) = 41.48
p = <0.0001
X2(6) = 27.58
p = 0.00011
X2(6) = 24.33
p = 0.00045
X2(6) = 91.70
p = <0.0001
X2(6) = 101.43
p = <0.0001
X2(6) = 66.73
p = <0.0001
X2(6) = 57.8
p = <0.0001
X2(6) = 63.93
p = <0.0001
X2(6) = 23.4
p = <0.00067
X2(6) = 10.39
p = 0.11
X2(6) = 13.61
p = 0.034
X2(6) = 43.56
p = <0.0001
24 36 48 60 72 84 96
Time (hAPF)

1330

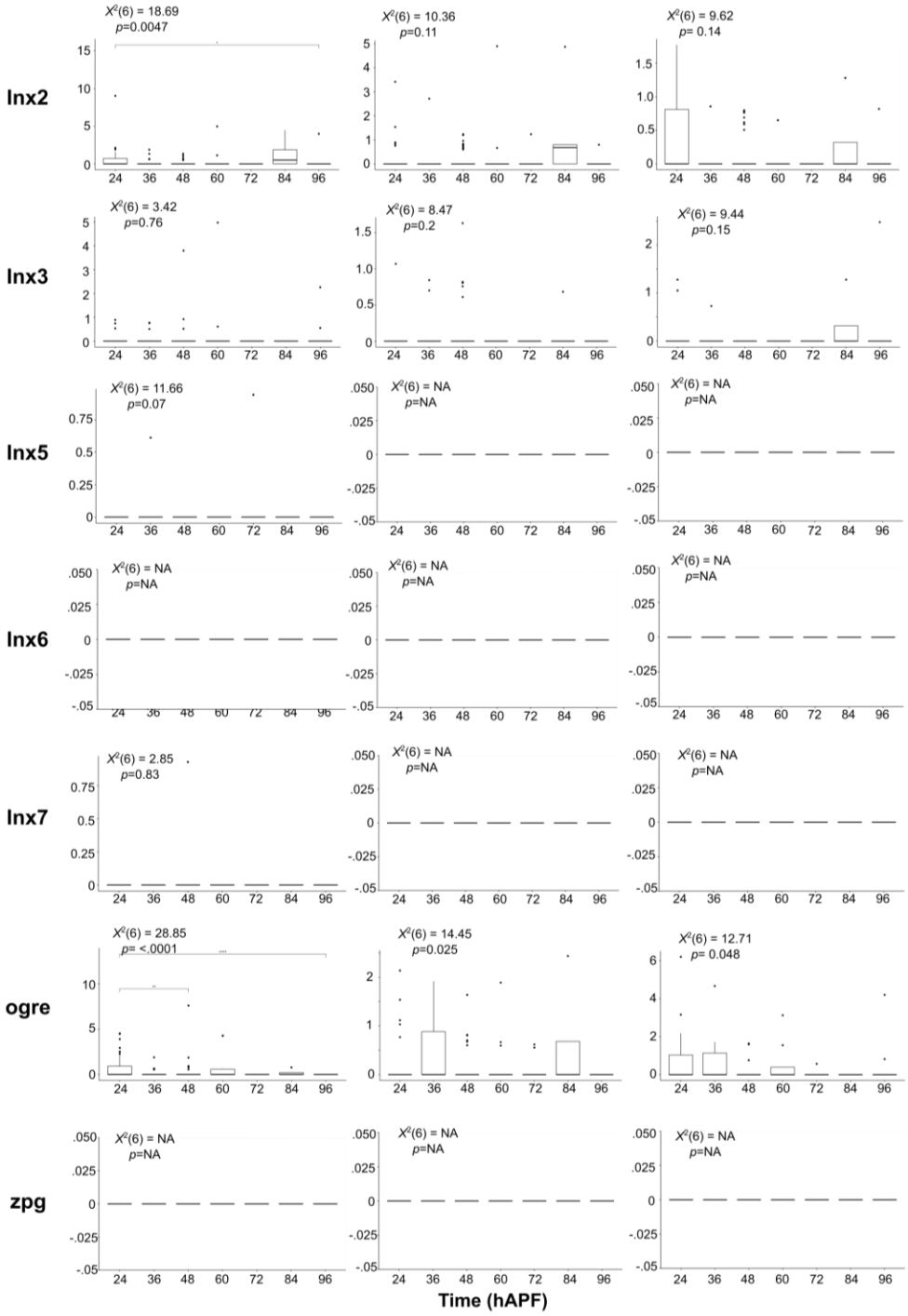

Figure 4 – figure supplement 1-3. Boxplots of all significant comparisons for genes listed in Figure 4. The first column show data for LC4, the second column for LPLC2, and the third column for LPLC1. An unpaired Kruskal-Wallis test was performed and chi square values and p values are shown above each figure. Each statistically significant test was followed up with a Dunn-Bonferroni multiple comparison test, with statically significant comparisons shown in each figure. * Indicates p < .05, ** indicates p < .005, *** indicates p < .0005.

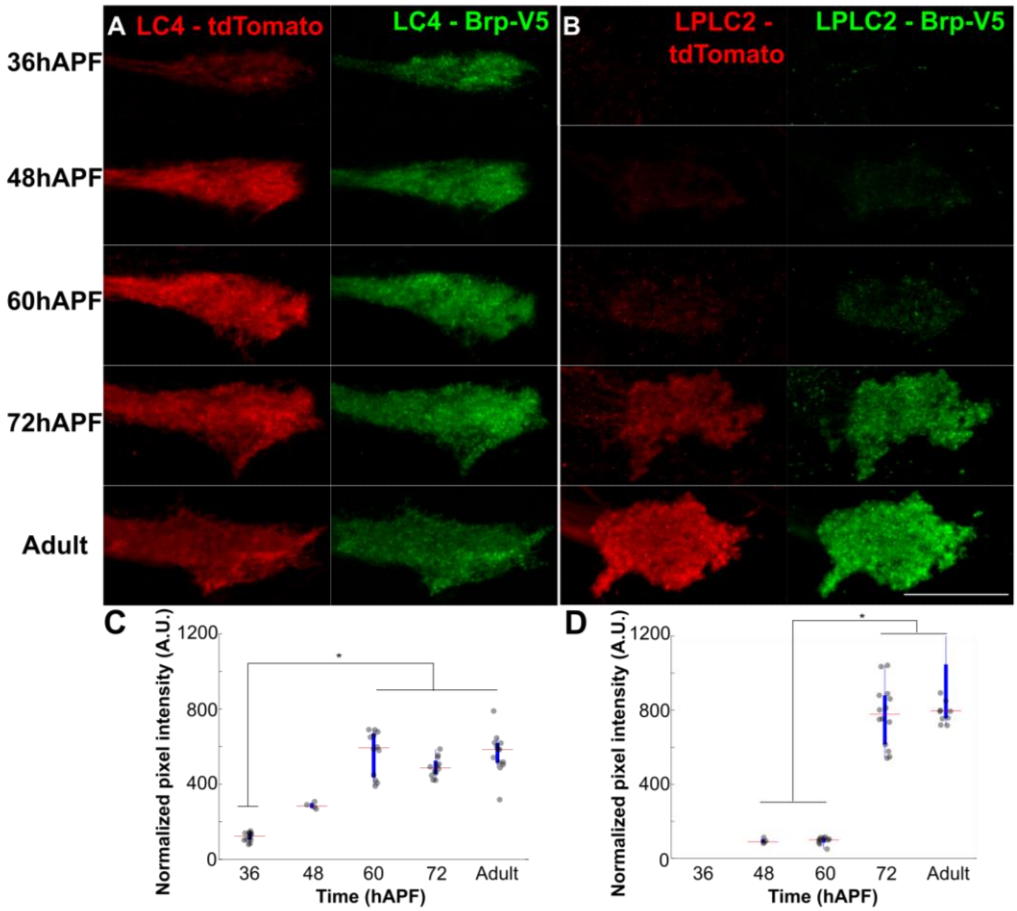

Figure 4 – figure supplement 4. Visualization of V5 tagged bruchpilot protein in select LCs populations using STaR.

(**A,B**) Max intensity projection images of LC4 (A) and LPLC2 (B) expressing tdTomato (red, left) and brp-smGdp-V5 (green, right) under endogenous brp promoter at distinct times during development. Scale bar, 20µm.

(C) Quantification of data from A. An unpaired non-parametric Kruskal-Wallis test was performed, $p = 2.42270 \times 10^{-7}$, followed by Dunn-Tukey-Kramer multiple comparisons test, * indicates $p < .05$. $N \geq 4$ half-brains per condition.

(D) Quantification of data from B. An unpaired non-parametric Kruskal-Wallis test was performed, $p = 5.33187 \times 10^{-6}$, followed by Dunn-Tukey-Kramer multiple comparisons test, * indicates $p < .05$. $N \geq 4$ half-brains per condition.

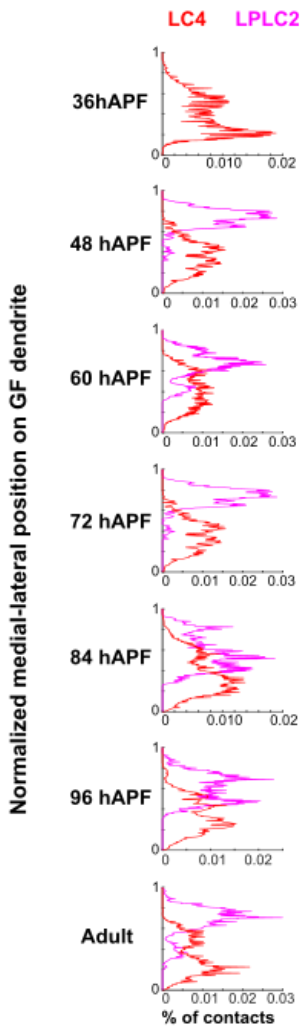

Figure 5– figure supplement 1. LPLC2 and LC4 contacts with GF show bias in dorsal-ventral localization.
Histograms of the average percentage of LC to GF dendrite colocalization along the normalized dorsal-ventral axis across development. The same images used for data analysis in Figure 5 are used here, with the difference being contacts are summed along the y-axis.

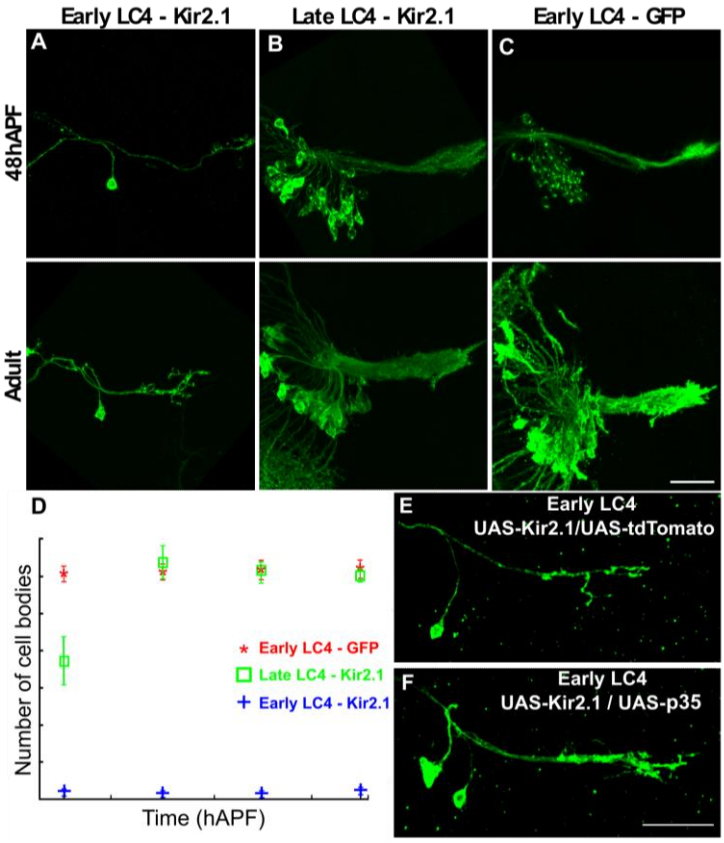

Figure 6 – figure supplement 1. Early expression of Kir2.1 causes LC4 cell death
(**A-C**) Max intensity projections of LC4 expressing Kir2.1 driven by LC4_4 driver (A) or LC4_1 driver (B), or LC4 expressing GFP driven by the LC4_4 driver (C). The top row 48hAPF, bottom row adult.
(D) Quantification of the number of LC4 cell bodies when expressing GFP (red) or Kir2.1 using the LC4_1 driver (green) or LC4_4 driver (blue). N $\geq$ 6 half brains per condition.
(**E, F**) Max intensity projections of LC4 expressing Kir2.1 and tdTomato (D) or p35 (E). Scale bar, 20um.